DEPARTMENT OF PHYSICS

TECHNISCHE UNIVERSITÄT MÜNCHEN

Bachelor's Thesis in Physics

Solar Atmospheric High Energy Neutrinos and SACSim

Desai, Kruteesh

PHYSIK DEPARTMENT

DEPARTMENT OF PHYSICS

TECHNISCHE UNIVERSITÄT MÜNCHEN

Bachelor's Thesis in Physics

Solar Atmospheric High Energy Neutrinos and SACSim

Hochenergieneutrinos von Sternatmosphären und SACSim

Author:	Desai, Kruteesh
Supervisor:	Prof. Dr. Elisa Resconi
Advisor:	Meighen-Berger, Stephan
Submission Date:	18.02.2021

PHYSIK
DEPARTMENT

I confirm that this bachelor’s thesis in physics is my own work and I have documented all sources and material used.

Munich, 18.02.2021 Desai, Kruteesh

Acknowledgments

I Hereby would like to thank Prof. Elisa Resconi for allowing me to have a chance of exploration in this field. The chance given to me have paved a great experience. The support and exposure I experienced during this study have encouraged me to explore even further in the field of astro-particle physics. I would also like extend my gratitude to Stephan Meighen-Berger for guiding me at every step of this wonderful journey. The lessons taught by him, from computer programming to presentation style, have been valuable to me. Even in the current situation of pandemic, the support that I received from Stephan have made this study possible and I will always be great full to Stephan and to Prof. Elisa Resconi for providing me with this opportunity.

Abstract

Solar Atmospheric neutrinos are produced due to cosmic ray interaction with the the sun's atmosphere. These neutrinos act as a background for various studies, such as dark matter interactions in the sun. They also act as a signal, which can be used to benchmark our understanding of the sun, as well as particle interactions and neutrino oscillations. In this study a new simulation model is developed to estimate the fluxes for various particles produced by impinging cosmic rays. SACSim(Solar Atmospheric Cascade Simulator) is a fast simulation model, providing an estimation of atmospheric cascade in stellar bodies. This makes it a useful tool to estimate the effects of new physics, interaction, oscillation, and density models. In this study a comprehensive analysis has been done on the modeling capabilities of SACSim to model Solar Atmospheric Neutrinos. Further areas of development and the probable steps for greater accuracy are discussed as well. The flux estimation from SACSim is comparable with previous studies done with various models and parameters.

Kurzfassung

Neutrinos werden in durch die Interaktion von kosmischer Strahlung mit Sternatmosphären produziert. Diese sind ein Untergrund für viele Studien neuer Physik, zum Beispiel dunkler Materie. Sie dienen auch als Signal, um die Präzision von Sonnen-, Teilcheninteraktions- und Oszillationsmodellen zu testen. In dieser Arbeit wird ein neues Simulationsmodell erstellt um die Flüsse verschiedener Teilchen, von kosmischer Strahlung in der Sonne produziert, abzuschätzen. SACSim (Solar Atmospheric Cascade Simulator) ist ein rapides Simulationsprogram, um diese Flüsse von stellaren Objekten abzuschätzen. Dadurch ist es ein nützliches Werkzeug um den Effekt neuer Physik, Interaktionen, Oszillationen und Sonnenmodelle zu testen. In dieser Arbeit wird eine Umfangreiche Studie von SACSim's Fähigkeit präsentiert Neutrinoflüsse von der Sonne zu modellieren. Es werden auch die nächsten Schritte, um die Präzision zu erhöhen, diskutiert. Die Abschätzungen der Flüsse mit SACSim sind vergleichbar mit früheren Studien.

Contents

1. Introduction

Solar atmospheric neutrinos are the centre of this study. SACSim (Solar Atmospheric Cascade Simulator) is designed to model particle cascades initiated in stellar bodies by impinging cosmic rays. There have been few studies conducted on the similar topic with different frameworks. The sun, as our closest stellar object, is the best candidate to conduct such a study . The sun blocks a certain amount of cosmic rays from reaching the earth , called cosmic ray shadow [1]. This is expected to cause an excess in the neutrino fluxes reaching to the earth because of the environment of the sun . The neutrino attenuation also play an important role in the final fluxes . These reduction though is majorly concentrated for cosmic rays passing through the core and it's near by region. Additionally, due to the low density in the atmosphere, compared to earth's atmosphere, the particles decay instead of interact. This causes a different spectral index for this region. The neutrino fluxes estimated by the simulation model developed can be used as a background to conduct further studies.

In this chapter the standard model with a special focus on neutrinos discussed. This lays foundation of this study. Cosmic rays initiate the particle cascades inside of the sun, while we employ the cascade equations to propagate them through the sun. The cosmic rays are the origin of the solar atmospheric neutrinos. The cosmic ray particles sometimes referred to as "Astro-messengers" are a useful tool for understanding the far fetched stellar bodies and their surroundings. Even though cosmic rays were discovered almost a century ago, their production and sources still remain a mystery. The study of their production and sources is confounded by external effects during their travels. Depending on their energies these effects vary and therefore the high energy regions are studied for looking at the objects outside of our solar system. In addition, the very high energy protons are not expected to be produced in solar system. In chapter 3 the nearest star to the earth has been simulated. This simulation provides an approximation of the sun to develop SACSim. The density of the sun that has been used for this simulation is developed from model-S and is provided at [2]. In chapter 4 the development of SACSim is discussed which is based on an open source program MCEq (Matrix Cascade Equation Solver) , which has various options for primary and interaction models. SACSim developed here, could be used flexibly for various scenarios and stellar objects . SACSim gives freedom to choose particles that are important for a particular study as well as to add theoretical particles such as dark matter candidates or super symmetric particles in the interaction models. Thus providing a new degree of freedom in applications.

1.1. The Standard Model

The Standard model describes the fundamental particles and interactions. Figure 1.1 describes the standard model where there are 3 parts

- **Bosons** : These are the force carrying particles. The strong mediator particles are 8 gluons, for the weak force there are $W^{\pm}$ and Z bosons and the electro-magnetic force carrying boson γ (photons) . These particles are not charged and have integer spin. These are the gauge bosons. The higgs boson is a scalar boson.
- **Leptons**: The $e^{\pm}$,$\mu^{\pm}$,$\tau^{\pm}$ are charge carrying particles that have half integer spin. The neutrinos of respective flavours and their anti particles do not carry charge and they have been only observed in left handed(right handed for their anti particles) helicity meaning the spin of the particle is always in opposite direction to the momentum(in same direction for anti neutrinos). The charged leptons can interact via Electromagnetic and weak force whereas the neutrinos can only interact via weak force according to the standard model.
- **Quarks** : These are the fundamental particle that make up the hadrons. The hadrons are the composites made of two or more quarks. The quarks have spin 1/2.

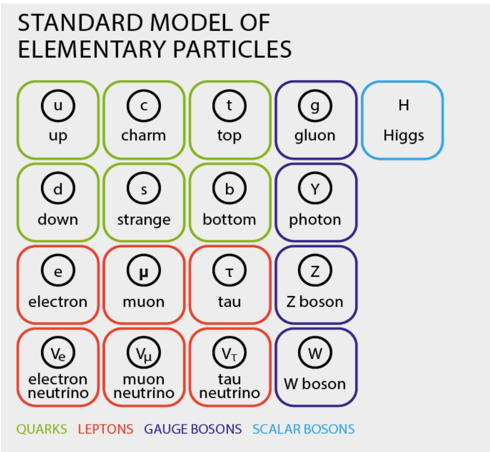

Figure 1.1.: The Standard Model

1.2. Neutrinos

Neutrinos are leptons. They were proposed by Pauli in 1930 in order to solve the problems with energy conservation and spin statistics in beta decay. They are observed only to exist in left handed helicity and their antiparticles in right handed helicity. They are divided into three families which are distinguished by the leptons e^{-},μ^{-}, τ^{-} i.e ν_e,ν_μ,ν_τ. They only interact via weak interactions. Because of their very small mass, detection through gravitational interactions has not been proven as of now. The detection through weak interaction can happen through neutral current channel with exchange of Z boson or through charged current with exchange of $W^{\pm}$ boson. Because of their behaviour of interaction they are proving to be Astrophysical messenger.

- **Charged current**: The neutrino passes through the detector transferring the fraction of its energy to a target particle. If the charged particle is sufficiently light weight then it would accelerate to relativistic speed and thus generate the cherenkov radiation which could be detected by photo multipliers. In this way the neutrinos could accelerate the e^-, μ^-, τ^-. The CC interactions follow reaction depicted in 1.1 and are sensitive to flavor of neutrino.
$$\nu_\alpha + N \longrightarrow \alpha^- + X \tag{1.1}$$
- **Neutral current**: The high energy neutrinos can interact with the hadrons in the medium via the reaction depicted in1.2 mediated by Z boson. NC interactions are insensitive to flavor of neutrinos.
$$\nu_\alpha + N \longrightarrow \nu_\alpha + X \tag{1.2}$$

The detectors such as IceCube detects neutrinos via both neutral and charged current interactions. The neutrinos produce their partner particles and X hadrons in the CC interaction. The X produce cascade signature. In the case of ν_μ CC, the μ^- are produced, which looses energy from ionization loses, bremstrahlung, photo-nuclear interactions. The combined Cherenkov light from the primary muon and secondary relativistic charged particles leaves a track-like pattern as the muon passes through the detector[3]. The e^- leaves a cascade signature form X hadronic cascade. The τ^- due to its short life and high reactivity with X hadronic cascade leaves double boom signature. These signatures are cherenkov radiation, the neutrinos accelerate the produced leptons to relativistic speeds depending on the incident neutrino's momentum. These signatures are depicted in the simulation Figure 1.2 [4]. The neutral current interactions are flavour insensitive and the charged current interactions are flavour sensitive, with this the signals could be categorized

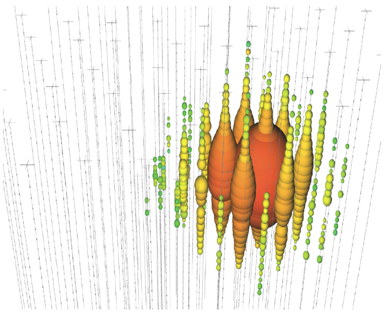

(a) ν_e signature : cascade

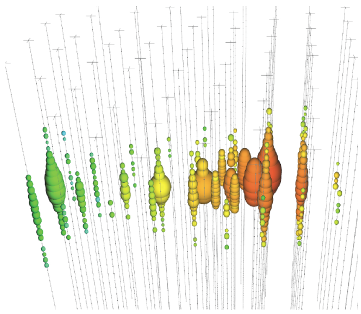

(b) ν_μ signature: Track

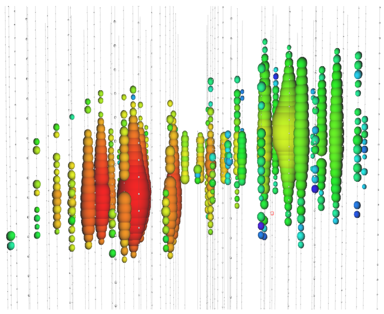

(c) ν_τ signature : double bang

Figure 1.2.: Simulation of signatures commonly observed by IceCube [4]

1.2.1. Neutrino Oscillation

The neutrinos as described before have three flavours based on their respective lepton family i.e. e^-, μ^-, τ^-. These flavours are mixture of mass eigenstates of so called ν_1,ν_2 and ν_3. In Quantum mechanics, the neutrino would be described by its wave function $\Psi(t)$ and the time dependent Schrodinger equation for a neutrino is described as below.

$$i\frac{d|\Psi(t)>}{dt} = H|\Psi(t)> \tag{1.3}$$

The general solution of eq. Equation 1.3 is

$$|\Psi(t)>= e^{-iHt}|\Psi(0)> \tag{1.4}$$

here $|\Psi(0)>$ is the initial state for which its could be assumed that the neutrino is in a flavour state l meaning $|\Psi(0)>=|\nu_l>$. The flavour states are related to the mass eigenstates by Equation 1.5

$$|\nu_l>=\sum_i U^*_{i,l}|\nu_i> \tag{1.5}$$

where the $U_{i,l}$ is an element of the unitary matrix

$$U = \begin{pmatrix} U_{1e} & U_{2e} & U_{3e} \\ U_{1\mu} & U_{2\mu} & U_{3\mu} \\ U_{1\tau} & U_{2\tau} & U_{3\tau} \end{pmatrix} \tag{1.6}$$

In the Equation 1.4 The Hamiltonian operator for a particle traveling through vacuum without any external potential could be written as the energy E. The energy for a particle could be written as Equation 1.7 under the natural units that is $\hbar$,c =1 .

$$E^2 = m^2 + p^2 \tag{1.7}$$

As of now it is well known that the neutrinos have very small mass thus the following could be written for the energy of the neutrino.

$$E = p(1+\frac{m^2}{p^2})^{1/2} \approx p(1+\frac{m^2}{2p^2}) \tag{1.8}$$

The time t in the similar manner could be also approximated under the natural units t=L. Now the probability of finding the neutrino in the flavour l′ after a length L could be described as following,

$$P(\nu_l \to \nu_{l'}) = \big| <\nu_l|e^{-i\Delta Hl,l'L}|\nu_{l'}> \big|^2 = \big| \sum_{i=1}^{3} U_{l,i}e^{-i\frac{\Delta mi,j}{2E}L}U^*_{l',j}\big|^2 \tag{1.9}$$

Now for the cases of j=i the mass difference would be 0 and the Unitary matrices has the characteristic of $\sum_i U_{li}U^*_{l'i} = \delta_{ll'}$ which makes the calculations easier as following,

$$P(\nu_l \to \nu_{l'}) = \big|\delta_{ll'} + \sum_{i\neq j} U_{li}e^{-i\frac{\Delta mi,j}{2E}L}U^*_{l'i}\big|^2 \tag{1.10}$$

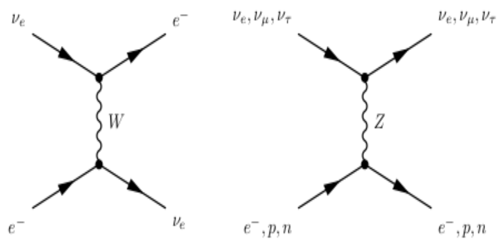

Figure 1.3.: Feynman diagrams of the coherent forward elastic scattering processes that generate the CC potential V^{CC} through W exchange and the NC potential V^{NC} through Z exchange.

The Equation 1.10 could be written For the scenario of three flavour mixing the unitary matrix could be defined with three components for propagation through vacuum are as following,

$$U = \begin{pmatrix} 1 & 0 & 0 \\ 0 & c_{23} & s_{23} \\ 0 & -s_{23} & c_{23} \end{pmatrix} \begin{pmatrix} c_{13} & 0 & s_{13}e^{-i\delta} \\ 0 & 1 & 0 \\ s_{13}e^{-i\delta} & 0 & c_{13} \end{pmatrix} \begin{pmatrix} c_{12} & s_{12} & 0 \\ -s_{12} & c_{12} & 0 \\ 0 & 0 & 1 \end{pmatrix} \tag{1.11}$$

The $c_{ij} = \cos\theta_{ij}$ analogous is the $s_{ij} = \sin\theta_{ij}$. Each matrix in Equation 1.11 represents Euler rotation, the δ in the second matrix is the CP violation phase which is responsible for the CP violation. The CP violation is the violation of charge conjugation and parity symmetry. The CP violation is yet to observed in neutrino. For the case of the matter the MSW(Mikheyev-Smirnov-Wolfenstein) effect is the responsible mixing mechanism[5]. The Hamiltonian for the case of the matter is different because of the neutrino interaction via CC and NC weak interactions with the matter. The Hamiltonian for a matter with varying mass density is as described in Equation 1.12

$$H' = H_0 + H_m = \frac{1}{2E}\left[U \begin{pmatrix} m_1^2 & 0 & 0 \\ 0 & m_2^2 & 0 \\ 0 & 0 & m_3^2 \end{pmatrix} U^* + \begin{pmatrix} V(x) & 0 & 0 \\ 0 & 0 & 0 \\ 0 & 0 & 0 \end{pmatrix} \right] \tag{1.12}$$

The V(x) is the so called the potential which is be different for the NC and CC. The phenomena responsible for the MSW effect is the forward coherent scattering of neutrinos via weak interactions with the matter, in the case of the sun Protons, electrons , neutrons. The effective hamiltonian for CC weak interacton is given in

$$H_{eff}^{CC}(x) = \frac{G_F}{\sqrt{2}}[\overline{\nu}_e(x)\gamma_\rho(1-\gamma^5)\nu_e(x)][\overline{e}(x)\gamma^\rho(1-\gamma^5)e(x)] \tag{1.13}$$

Where the x is the distance and the γ^ρ and γ^5 are γ matrices. The Equation 1.14 depicts the hamiltonian for the NC weak interactions.

$$H_{eff}^{NC}(x) = \frac{G_F}{\sqrt{2}} \sum_{\alpha=e,\mu,\tau} [\overline{\nu}_\alpha(x)\gamma^\rho(1-\gamma^5)\nu_\alpha(x)] \sum_f [\overline{f}(x)\gamma_\rho(g_V^f - g_A^f\gamma^5)f(x)] \tag{1.14}$$

The $(1-\gamma^5)$ factor in Equation 1.13 and Equation 1.14 is for left handedness of neutrinos(or right handedness for anti-neutrinos), where as g_V^f,g_A^f are for Vectorial and Axial quantities depicitng Fermi and Gammow teller transition respectively[6]. The $V^{CC} = \sqrt{2}G_F n_e$ and $V^{NC} = -\frac{\sqrt{2}}{2}G_F n_e$ where the n_e is electron number density of the medium, $G_F = \frac{\sqrt{2}g^2}{8M_W^2}$ is Fermi's constant [7], here the g is a coupling constant and M_W is mas of $W^{\pm}$ boson. The values of V^{CC} and V^{NC} are calculated from the effective hamiltonians for CC and NC weak interactions. The Feynman diagrams for both interactions are drawn in Figure 1.3. The Equation of motion for the matter would be written as Equation 1.15.

$$id_x\Psi = H'(x)\Psi \tag{1.15}$$

Where the Ψ is the wave function for the neutrino and the H'(x) is the effective hamiltonian with the potentials for NC and CC mentioned above. The solution of the Equation 1.15 as Equation 1.4 with the variable x is in vector form in flavour basis meaning $\Psi = (\nu_e, \nu_\mu, \nu_\tau)$. In this study and the SACSim being developed, the neutrino oscillations in matter have not been incorporated yet. The application of the MSW effect and calculation of survival probabilities for all neutrino flavours could be done with the help of above described fundamental formulas. The incorporation of neutrino oscillations would make the SACSim a bit slower but would give more accurate results of the fluxes. As the authors in [8] conclude from their results for solar atmospheric neutrinos in the high energy range have significantly suppressed oscillations in the matter and could be approximated with the neutrino oscillation in vacuum as Equation 1.16-Equation 1.20 with sun-earth distance that a neutrino would travel, approximated with $L \approx 215R_{sun}$.

$$P_{ee} \approx 0.57 \tag{1.16}$$

$$P_{e\mu} \approx 0.43c_{23}^2 \tag{1.17}$$

$$P_{\mu\mu} \approx 0.57c_{23}^4 + s_{23}^4 \tag{1.18}$$

$$P_{\mu\tau} \approx 1.57c_{23}^2 s_{23}^2 \tag{1.19}$$

$$P_{e\tau} \approx 0.43s_{23}^2 \tag{1.20}$$

The θ_{23} having larger uncertainties is the unknown variable in the Equation 1.16-Equation 1.20.The oscillation parameters used here are $\delta m^2 = 7.92(1 \pm 0.09)^{-5}eV^2$, $\Delta m^2 = 2.6(1^{+0.014}_{-0.15}) \times 10^{-3}eV^2$, $\sin^2\theta_{12} = 0.314(1^{+0.18}_{-0.15})$, $\sin^2\theta_{23} = 0.45(1^{+0.35}_{-0.20})$, $\sin^2\theta_{13} = (0.8^{+2.3}_{-0.8}) \times 10^{-2}$, where the $\delta_{CP} = 0$, $\sin\theta_{13}{}^2 = 0$ and normal mass hierarchy has been assumed in [8]. normal hierarchy is the $m_2 \approx m_1 < m_3$, whereas the inverted hierarchy is $m_2 \approx m_1 > m_3$.

2. Cosmic Rays

The cosmic rays are playing an important role in field of astrophysics and particularly astro-particle physics. They are so called messengers because of the information that could be extracted about the source of these particles or the medium they have traveled through. Inter planetary (in solar system) exploration is mainly executed by the probes but for the case of inter galactic or extra galactic exploration the electromagnetic radiation, gravitational waves, neutrinos and cosmic rays are used. The electromagnetic radiation that is photons does not get affected by the external electromagnetic fields therefore they are reliable source to observe the stellar objects and exoplanets radiating or reflecting EM waves, at the same time the photons get quickly attenuated, therefore reducing their reach. The gravitational waves due to their nature require highly sensitive equipment this limits the observations to the massive objects such as Black-holes and neutron stars. The neutrinos as discussed in the chapter 1 interact via weak force meaning the external electromagnetic field does not affect the path making them also a reliable messenger but they are difficult to extract information from.

2.1. Primary Cosmic Rays

The primary flux is what we call cosmic ray particle's influx. They are about 90% protons, 9% alpha particles and the rest are heavy nuclei such as C,N,O,Fe etc. The primary flux have energies higher than the mass of respective particle/nuclei masses extending from about few GeV to 10^{20} eV. It has been known through various experiments and detectors that the primary flux predominantly originates from outside of the solar system but from within the Galaxy. This has been determined by the correlation of solar particle influx with the Solar activity and anti correlation of the rest of primary flux or cosmic ray influx.

Figure 2.1 depicts this phenomena where the abundances in cosmic rays and the solar system relative to the Carbon with respective to the Nuclear charge has been shown. This depicts the higher abundance of heavier elements in cosmic rays in comparison to the Solar system material. That implies the composition of the source. The heavier elements are primarily produced because of the interaction of Cosmic ray interaction with the Interstellar Medium (ISM). [9]

Figure 2.2 shows the differential fluxes of various particles existing in Primary flux. This plotted in [10] from data of various detectors such as AMS02 , PAMELA, BESS etc.

In addition to that the gyro radii of the particles which has been detected to be greater than the size of the Galaxy[9]. The gyro radius is the radius of circular motion of charged particle in external magnetic field. Through Lorentz force equating to the centrifugal force this radius could be extrapolated for a particle of mass m, charge q and velocity v for a galactic magnetic

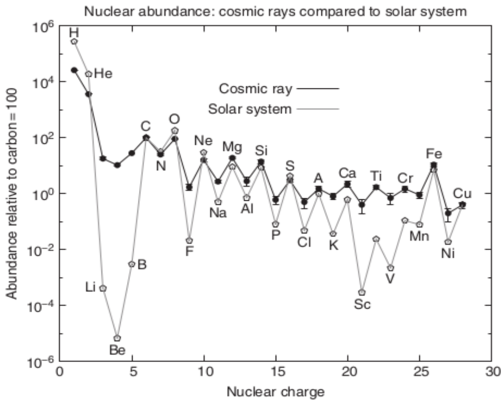

Figure 2.1.: The cosmic ray elemental abundances measured on Earth (filled symbols connected by solid lines) compared to the solar system abundances (open symbols), all relative to carbon = 100.[9]

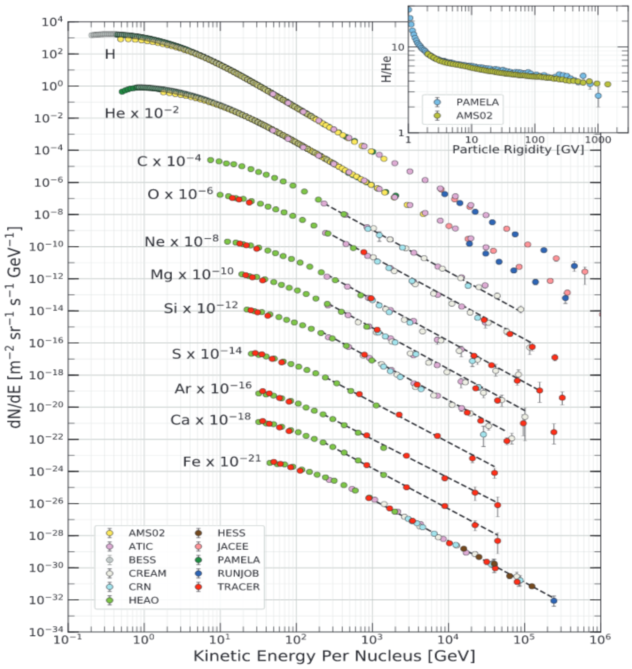

Figure 2.2.: Fluxes of nuclei of the primary cosmic radiation in particles per energy-per-nucleus are plotted vs energy-per-nucleus. The inset shows the H/He ratio at constant rigidity [10]

field B for the case of cosmic ray.

$$r_L = \frac{mv}{qB} = \frac{pc}{ZeB} \tag{2.1}$$

The rigidity above mentioned is computed through multiplying the magnetic field to the gyro-radius as described in the equation

$$R = r_L B = \frac{pc}{Ze} \tag{2.2}$$

From the equation Equation 2.2 it could be deducted that as the momentum of the particle increases the rigidity factor also increases. For particles above 200 GeV energy have greater rigidity which implies greater gyro-radius implying the lesser effect of magnetic field, in our case magnetic field of the Sun, on the Cosmic ray particles.[11] Therefore in our study the focus has been more towards the energy limits of above 200 GeV where the magnetic effects could be neglected.

2.1.1. Energy Spectra

Th energy spectra of particle flux is the power law particle differential flux follows in relation to the energy E

$$\frac{d\Phi_i}{dE} \propto E^{-\gamma} \tag{2.3}$$

As Equation 2.3 describes the γ is the so called Energy spectra of particular particle i follows. The proportionality components of this relation are constant with respect to the energy.

$$\Phi_i = \frac{1}{\gamma} \frac{d\Phi_i}{d \ln E} \tag{2.4}$$

The Equation 2.4 provides a power law relation of the total flux with energy. The γ is a so called Integral Spectral index or sometimes referred to as energy spectrum. The energy spectrum is the quantity that is used for analysis of the differential or total fluxes for a given system. Secondaries cosmic rays as name describes are the fluxes of the particles produced by the interaction of cosmic ray with the interstellar medium, $\overline{P}$,$\overline{n}$ are examples of such secondary cosmic rays.
The CR particles both the remaining primary and the secondary CRs then interact with the atmospheric particles and molecules or decay into further particles such as leptons which are called secondaries. At the end most of the heavier particles would interact or decay into stable particles such as neutrons. This is called cascade effect or air shower, for the case of the earth Figure 2.3. The cascade could be also divided into two categories

- Electromagnetic Cascade : The electrons ,produced as secondaries, lose energy via various phenomenon such as bremstrahlung. These in turn generates a cascade of electromagnetic radiation [12] which is then called electromagnetic cascade

- Hadronic Cascade: The secondaries produced further interact or decay and make cascade of hadronic products that is the so called 'Hadronic cascade'.

As our study is more concentrated for the neutrinos which are mainly produced in the hadronic cascade branch the EM cascade has been neglected here.

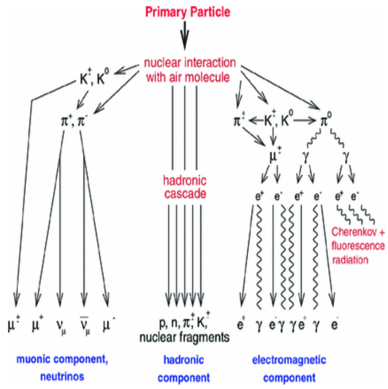

Figure 2.3.: A depiction of air showers in Earth's atmosphere[13]

2.2. Cascade Equations

The cascade equations are the equations describing the cascade effect mentioned above. The cascade equations are the coupled differential diffusion equations for the fluxes of the particles in concern.

$$\frac{d\Phi_i(E)}{dX} = -\frac{\Phi_i(E)}{\lambda_{i,int}} - \frac{\Phi_i(E)}{\lambda_{i,dec}(X)} + \sum_j \int_{E'>E} \frac{\Phi_j(E')}{\lambda_{j,int}} \frac{dn_{j(E')\to i(E)}}{dE} dE' + \sum_j \int_{E'>E} \frac{\Phi_j(E')}{\lambda_{j,dec}(X)} \frac{dn_{j(E')\to i(E)}}{dE} dE' \tag{2.5}$$

The Equation 2.5 is a cascade equation ofr a particle i for energy E. The j in the equation stands for the set of the particles considered in a system. The first two terms with the negative sign are the so called loss terms whereas the last two terms are the gain terms. The variable X is the slant depth .

$$X = \int_0^h \rho(l)dl \tag{2.6}$$

As Equation 2.6 describes the slant depth has units g/cm^2 . It describes the amount of matter that a particle encounter for a given path length h through an object with variable mass density dependent on the depth. The X brings a simplified nature to the cascade equations in contrast to the normal length and allows easier analysis because it removes the dependence over the density and could be generalized.

2.2.1. The Loss terms

The loss terms describe, as name suggests, the loss of flux through various interaction and decay channelsEquation 2.7

$$\frac{d\Phi_i(E)}{dX} \supset -\frac{\Phi_i(E)}{\lambda_{i,int}} - \frac{\Phi_i(E)}{\lambda_{i,dec}(X)} \tag{2.7}$$

The Equation 2.8 describes the interaction length, it has units g$/cm^2$ the same as slant depth X.

$$\lambda_{i,int} = \frac{\rho}{\eta\sigma_{i-atm}^{inel}} \approx \frac{Am_p}{N_A A^{2/3}\sigma_{p-p}^{inel}} \tag{2.8}$$

The interaction length is $\rho\times$M(mean free path) meaning the average amount of matter, particle i would pass through before interacting. The interaction length is independent of density of material but dependent on the average mass number A i.e. type of material. For the case of the sun it could be calculated with the atomic composition . The sun has 73.81% H, 24.85% He and 1.34% heavy metals[14]. These composition leads to A=1.9465

$$\sigma_{i-atm}^{inel} \approx A^{2/3}\sigma_{p-p}^{inel} \tag{2.9}$$

The Equation 2.9 is an approximation to estimate the total inelastic cross section from $\sigma_{pp}^{inelastic}$ and mass number A[15]. This allows to modify the interaction length for the sun as Equation 2.10

$$\lambda_{i,int} \approx \frac{A^{1/3}m_p}{N_A\sigma_{p-p}^{inel}} \tag{2.10}$$

The inelastic cross section for pp collision are available via various interaction models such as SIBYLL 2.3 cpp. The SIBYLL 2.3 c is hadronic interaction model is mainly used for cosmic ray air shower simulation. While the general features of QCD like quark confinement, multiple interactions and jet production are included in the model, particular features that are relevant for the development of air showers, like diffraction dissociation and forward particle flow are implemented in more detail [16]. With the parameterization mentioned in Equation 2.10 the SIBYLL 2.3 cpp model has been used which is developed for pp interaction hense the name SIBYLL 2.3 cpp. The excess seen in Figure 2.4 in the low energy region for SIBYLL 2.3 cpp is due to the low energy extension which is not relevant for this study therefor could be neglected. If this energy range is required for further study than another hadronic interaction model with parameterization mentioned above should be used. The Figure 2.4 shows the inelastic cross section for pp collision with data from Particle Data Group [17] as well as with the various interaction models available such as SIBYLL 2.3, QGSJet, EPOS-LHC after applying the Equation 2.9 parameterization because they are developed for the air shower simulations or detector simulation. From Figure 2.4 it could be concluded that the SIBYLL 2.3 cpp is a good approximation for the energy range greater than 100 GeV. The inelastic cross sections derived from the other interaction models are also good approximation implying the validation of Equation 2.9 .

$$\lambda_{i,dec}(X) = c\tau\beta\frac{E}{m_i}\rho(X) \tag{2.11}$$

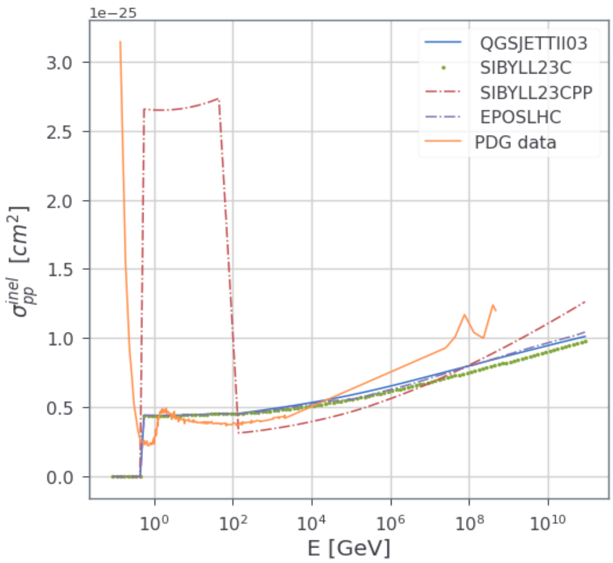

Figure 2.4.: Inelastic cross section for pp interaction obtained via application of Equation 2.9 for various interaction models available in MCEq after applying the parameterization from Equation 2.9 as well from data files provided by[17](orange). The discrepancy in SIBYLL 2.3 cpp for low energy region is neglected for this study because of the energy range in focus.

The Equation 2.11 describes the decay length of a particle i with mass m_j and lifetime τ at energy E. whereas the c is speed of light and β is ratio of particle velocity to the c . The decay length is dependent on the mass density of target or the matter the particle is passing through. The decay length also has the same dimensions as slant depth X.

2.2.2. The Gain Terms

The gain terms describe the production of a particular particle through various interaction or decay channels of particles considered for a system.

$$\frac{d\Phi_i(E)}{dX} \supset \sum_j \int_{E'<E} \frac{\Phi_j(E')}{\lambda_{j,int}} \frac{dn_{j(E')\to i(E)}}{dE} dE' + \sum_j \int_{E'<E} \frac{\Phi_j(E')}{\lambda_{j,dec}} \frac{dn_{j(E')\to i(E)}}{dE} dE' \tag{2.12}$$

The Equation 2.12 are the so called gain terms which are from two branches the interaction term and the decay term. The interaction term describes particle production from interactions of other particles in a particular system. In the Equation 2.12 the first is the gain terms where the $\Phi_j(E')$ is the flux of the so called parent particle of type j ,the $\lambda_{j,int}$ is interaction length of the particle j in the system. The $\frac{dn_{j(E')\to i(E)}}{dE}$ is the yield.

$$\frac{dn_{j(E')\to i(E)}}{dE} = \frac{1}{\sigma_{total,j}} \frac{d\sigma_{j(E')\to i(E)}}{dE} \tag{2.13}$$

The Equation 2.13 shows that the yield has mass dimension E^{-1}. The yield is a fraction of the total inelastic cross section consumed for production of particle i per energy . In this manner the integral carried out for the energies E′ higher than E in Equation 2.12. The lower limit of E for the integral is a trivial limit, because of the energy conservation the parent particle j must have greater energy E′ than the energy E of particle i. These energy integral in the literature are called the "Z- kernel" or "spectrum weighted momentum" to make calculations easier [9]. The Z kernels are normalized with the energy of the parent particles as depicted in the Equation 2.14

$$Z_{ih} = \int x^{\gamma} \frac{dn_{ih}}{dx} dx \tag{2.14}$$

where the x=E_i/E_j and the γ is the unknown spectrum index that the flux of the particle i (child particle) follows. Analogously this is carried out for all the possible interaction channels which produce the particle i and are added hence the summation over j. In the similar manner the decay terms are defined for the production of particle i via decay of particle j with the same integral limits and summation but with the decay length and decay yields.

2.2.3. Energy Loss terms

The charged particles lose energy while traveling through matter. These lose happen because of various phenomenon such as radiation, bremstrahlung, ionization etc. The ionization losses are described via the Bethe-Bolch equation .[18]

$$\left\langle -\frac{dE}{dX} \right\rangle = \alpha^2 2\pi N \lambda_e^2 \frac{Z m_e}{A\beta^2} \left[\ln \frac{2m_e \beta^2 \gamma^2 E'_m}{I^2(Z)} - 2\beta^2 + \frac{1}{4}\frac{E_m^{2\,\prime}}{E^2} - \delta \right] \tag{2.15}$$

In the Equation 2.15 α is the fine structure constant, Z and A are atomic number and mass number of the matter, β is the v/c of incident particle, m_e is mass of the electron, λ_e is compton wavelength of the electron , γ is the lorentz factor for the incident particle, I(Z) is mean ionization potential of the medium,δ is the density correction and E'_m is the maximum energy transferable to the electron as described in the Equation 2.16

$$E'_m = 2m_e \frac{p^2}{m_e^2 + m^2 + 2m_e\sqrt{p^2 + m^2}} \tag{2.16}$$

In the Equation 2.16 the p and m are the momentum and mass of incident particle respectively. The Bethe-Bloch equation is based upon the Rutherford differential cross section of the charged particles in the matter. Since the electron are not always free in matter the E'_m has to be bounded and it depends on the atomic and bulk structure. The ionization loses are approximated with a function a(E) in the Equation 2.17 for $\mu^{\pm}$

$$\left\langle -\frac{dE}{dX} \right\rangle = a(E) + b(E)E \tag{2.17}$$

b(E) is the sum of $e^{+}e$ pair production, bremsstrahlung, and photo-nuclear contribution in the energy loss. The a(E) and b(E) are both slowly varying functions. The energy at which both

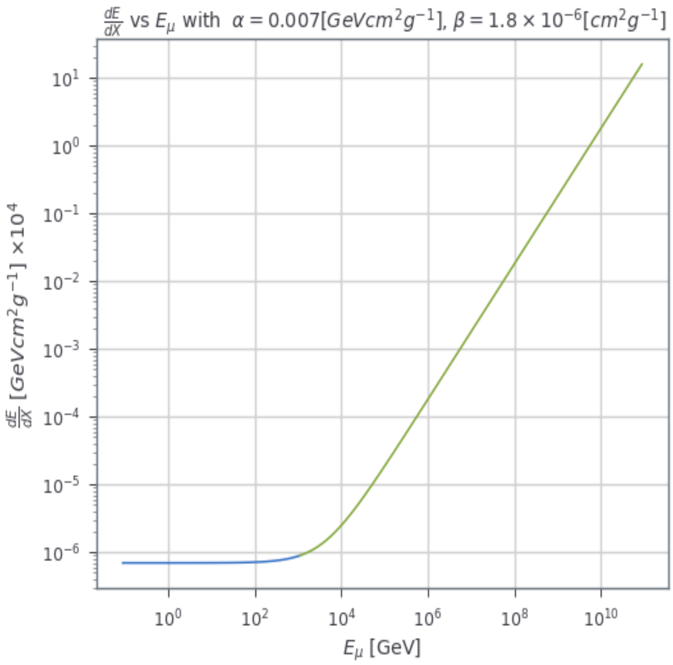

Figure 2.5.: Energy loss term with respect to the E_μ with parameters $\alpha = 0.007$ $[GeVcm^2g^{-1}]$ and $\beta = 1.8 \times 10^{-6}$ $[cm^2g^{-1}]$ for the case of 78% hydrogen and 28% helium composition of the sun. The blue region depict (ionization losses) a(E) dominant area and the greed curve represents the b(E) dominant region

terms are equal is called critical energy $E_c = a(E_c)/b(E_c)$. The ionization loses are dominant below the critical energy whereas above critical energy the radiation loses are dominant.[19].

As Figure 2.5 depicts the energy loss with respect to the slant depth i.e $\frac{dE}{dX}$ is approximately from 10^{-6} to 10^5 [GeV cm^2 g^{-1}] over the energy range. As the [20] concludes the production of neutrinos is concentrated near the surface i.e the slant slant depth in this region being in the range 0-250 $[gcm^{-2}]$. This would take the absolute loss in energy i.e ΔE in the range 10^0 to 10^8 [GeV] which is maximum approximately 0.01 times the energy i.e 1%. Therefore the energy loss terms have been neglected in this study. The low energy region where the energy losses are about constant is where the a(E) or α is dominating meaning the ionization losses are dominant in this region. After the critical energy approximately in 10^3 GeV order the b(E) or β is dominant where the energy losses are rapidly increasing. This region is dominated by the energy losses from pair production, bremstrahlung and as such mechanisms.

3. The Sun

The Sun , the closest star to us this makes it the perfect candidate to study inner workings of a star. Over the years various observatories have conducted several studies regarding the sun and the inner structure of the sun. From these studies standard models have been developed to describe the sun.

3.1. Standard Models

As it is well known that the sun and such stars are massive objects made of plasma which is globally neutral in terms of electrical charge. The stellar models are an attempt to describe the physical quantities such as pressure, temperature and chemical properties t every point of the star in focus. This is done by solving stellar equilibrium equations. The stars are thought to be at thermodynamical equilibrium and follow black body radiation because of the efficiency of photon nuclear interactions. Thus the thermodynamic properties of plasma are calculated as function of chemical composition and two physical quantities through equations of state (EoS)[21]. Due to spherical symmetry of the sun and because of the hydrostatic equilibrium, the pressure at any point in any particular shell of small thickness balances the gravitational contraction for a stable star. This allows to treat the sun as combination of shells. This simplifies the calculations as Equation 3.1 depicts. The below explanation is based on the [21] where the author describes the process in depth.

$$\frac{dm(r)}{dr} = 4\pi r^2 \rho(r) \tag{3.1}$$

The ρ is mass density and the r is local radius. As described above the pressure would be balanced out with the gravitational contraction therefore the Equation 3.2 could be written.

$$\frac{dP(r)}{dr} = -G\frac{m(r)\rho(r)}{r^2} \tag{3.2}$$

The above described two equations are the fundamental equations upon which the Standard Models are attempted to be developed. These both have some unknown variables such as $\rho(r)$,P(r) and m(r). The thermal equilibrium for such a shell could be written with the Luminosity L(r) as Equation 3.3

$$\frac{dL(r)}{dr} = 4\pi r^2 \rho(r)\epsilon(r) \tag{3.3}$$

where ϵ is the specific energy generation rate (erg/gs). The thermal equilibrium mentioned above happens due to the amount of energy per unit time (luminosity) which exits from a given shell direct outward is equal to the amount of energy which enters in the shell plus the energy possibly produced in the shell itself. This phenomenon could be described by the $\epsilon(r)$ which is the energy produced or lost per unit and per unit mass. The total amount of photon-matter interaction processes, which remove energy from the outgoing flux, is called "opacity".

$$\kappa = \frac{1}{\rho\lambda_\gamma} \tag{3.4}$$

At thermodynamic equilibrium the quantity κ the so called opacity ($cm/$g) is defined and the λ_γ is the mean free path of photon inside the star. This mean free path is the result of photon matter interactions. The opacity is stronger where the matter is not completely ionized. The dominant energy transport mechanism is assumed to be the photon matter interactions which allows to relate the temperature gradient with energy flux with Equation 3.5 which is called 'energy radiative transport equations'.

$$\frac{dT(r)}{dr} = -\frac{3\kappa\rho(r)}{16\pi ac}\frac{L(r)}{r^2T(r)^3} \tag{3.5}$$

The initial conditions used to solve these set of equations mentioned above are mainly divided in two variations (i) low metalicity or low Z , (ii) high metalicity or high Z i.e. the fraction of metal abundance present at the time of formation of a star. The X, Y correspond to the fractional abundance of H and He respectively, meaning X+Y+Z=1. The Standard Solar Model developed this way provides us important thermodynamic quantities such as entropy, temperature profile, density profile which help to estimate the observable such as neutrino flux. Upon comparing the SSM with the helioseismic observations it has been concluded and well known that the photospheric He abundance from SSM is little lower as well as the convection zone surface radius [22]. This is called 'Solar Abundance Problem'

The Helioseismology is the study of stellar objects through particle oscillations in more common words through speed of sound. The Helioseismic models of the sun make use of the speed of sound to be more precise pressure oscillation measured via satellite. The SOHO(Solar and Heliospheric Observatory) satellite is such satellite. The GOLF(Global Oscillations at Low Frequencies) instrument mounted on the SOHO measures p-waves concerned with thew solar core as well as the Michelson Doppler Imager(MDI) focused on photospheric measurements. These observational data would be converted to the density profile, temperature profile etc. to conduct further studies for the stellar structure and to develop precise Standard Solar Model. In this study Model S developed by Christensen-Dalsgaard, J. et .al has been used. The model S has been developed with The Global Oscillation Network Group (GONG) data.[2]. This model was developed with the basic parameters that are accurately known such as $M_{sun} = 1.989 \times 10^{33}$ g , luminosity $L_{sun} = 3.846 \times 10^{33}$ ergs s^{-1} , radius $R_{sun} = 6.96 \times 10^{10}$ cm as well as the $Z/X = 0.0245 \pm 0.005$. The model was calibrated to depict the current state of the sun. The Figure 3.1 depicts the density variation with respect to the r=R/R_{sun} the R_{sun} taken here is 6.957×10^{10} cm and data used is provided at the website mentioned with [2]. In the [20] the author has compared the model S with the models from [23] Serenelli ,A. et al. as well as model developed by R.F. Stein et al.[24] and concluded that they are very similar.

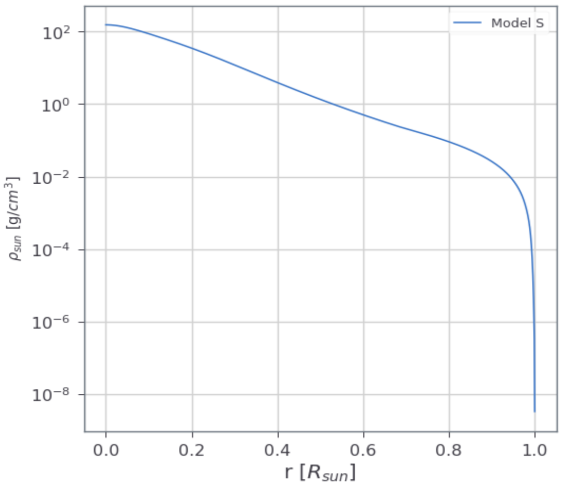

Figure 3.1.: ρ_{sun} mass density of sun [g/cm^3] from Model S

The passage through the sun has been parameterized with the straight path passing through the sun with various impact parameter b i.e the shortest distance from the centre of the sun a particle would achieve while traveling on this straight path through the sun a depicted in the Figure 3.2.

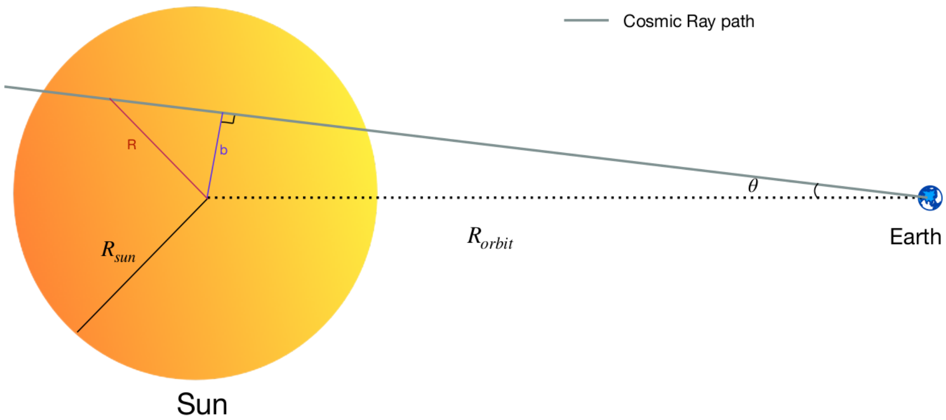

Figure 3.2.: A depiction of geometry used in this study for CRs traveling through the sun

Such geometry provides us with the flexibility to analyse the observables for various impact paramters which could be again parameterized to the angular to the angular profile the sun would have from a given point at the surface of the earth as Equation 3.6 ,

$$\sin\theta = \frac{b \cdot R_{sun}}{R_{orbit}} \tag{3.6}$$

The angular resolution of the sun could be described by the same Equation 3.6 for impact parameter b=1. This would lead us to the $2\theta = 0.54°$ for $R_{orbit} = 1.47 \times 10^{13}$ cm with approximating the earth as a point like object compared to the sun.

4. SACSim

The Solar atmospheric neutrinos in the high energy regime are the focus of SACSim (Solar Atmospheric Cascade Simulator). In particular the energy range from 200 GeV to 10^7 GeV. SACSim is based on open source code named MCEq (Matrix Cascade Equation Solver)[25]. MCEq is a tool to numerically solve cascade equations that describe the evolution of particle densities as they propagate through a gaseous or dense medium. The main application are particle cascades in the Earth's atmosphere. Particles are represented by average densities on discrete energy bins. The results are differential energy spectra or total particle numbers. Since this tool has been developed primarily for the Earth's atmosphere in order to apply it for solar atmosphere several modifications have been done which are discussed in this chapter. The First is that MCEq has flexibility to choose various parameters and interaction models. In this chapter the impact region is referred to region of impact parameters b, e.g The near surface impact region is implied to the region of impact parameter b=0.9 to 1.0. The primary energy or prime energy is the energy of parent particles that produce the particle in focus sometimes referred to as child particle that has energy denoted by E_{sec} or E_ν(for neutrinos) . The calculations are done in rest frame of medium.

4.1. MCEq as matrices generator

MCEq as name suggests uses matrix form of the coupled cascade equation. This enables the simulation of a cascade more effectively and manageable. As pointed out above the fluxes calculated from this tool are average fluxes over the predefined energy bins therefore they are differential fluxes instead of absolute. Therefore the analysis done over the results for the SACSim developed are also based on the differential fluxes.

$$\frac{d\Psi}{dX} = \left[[C-1]L_{int} + [D-1]\frac{L_{dec}}{\rho(X)}\right]\Psi \tag{4.1}$$

The Equation 4.1 describes the matrix form of the Equation 2.5 where the Ψ is a vector composed of differential fluxes over energy bin defined in MCEq for all cascade particles in focus.

$$\Psi = (..., \frac{d\Phi_i}{dE_i}, ..., \frac{d\Phi_j}{dE_j}, ...)^T \tag{4.2}$$

The Equation 4.2 describes the vectorial form of the Ψ where every particle included in the system have differential over the predefined energy bins. The predefined energy bins are ranging from 0.0089 GeV to 8.9×10^{10} GeV. It has 121 elements in this range meaning the vectorized differential fluxes for a particle i have length of 121 elements and this would be for all the elements included in the model. The MCEq has 81 cascade particles and composites from photons to baryons such as Λ^0. These have various particles that are distinguished on the basis of helicity and also some are categorized by the parent particles they were produced, in order to provide a tool for analysis of a specific interaction or decay channel. Amongst these in the simulation developed 22 particles have been included. In order to understand the effect of this short listing the total inelastic cross sections for PP collision and the total inelastic cross section after integrating the yields of proton-h interactions with interaction model based on PP collision , where h being the 22 particles and composites included in the SACSim have been compared. The Figure A.2 depicts negative deviation from the MCEq in total inelastic cross section for a proton. The negative values are because of the short listing from 81 particles to 22 particles and the 0.3% deviation or 0.003 of absolute deviation shows that the 22 particles are the most relevant particles for the situation of cosmic ray interacting with solar atmosphere both primarily made of protons. The interaction yields mentioned above are from the Matrices composed of interaction yields for various interaction channels.

$$C = \begin{pmatrix} c_{l\to j} & c_{l\to l} & c_{l\to k} & . & . & . \\ . & . & . & . & & \\ . & . & . & & & \\ c_{k\to j} & c_{k\to l} & c_{k\to k} & . & . & . \end{pmatrix} \tag{4.3}$$

The $c_{i\to h}$ are again matrices which are triangular in nature and consist of interaction yields for that particular interaction channel over the energy bins for combinations of energies of parent child particles. The upper triangular nature of these matrices arises because of the lower limits of energy described for the integral in the Equation 2.5. The integral in the Equation 2.12 for the interactions and decay terms are converted into the summation because of the energy bin usage.

$$c_{i\to h} = \begin{pmatrix} c_{i\to h}(E_{i,1}, E_{h,1}) & . & . & c_{i\to h}(E_{i,1}, E_{h,n}) \\ 0 & . & . & . \\ 0 & 0 & . & . \\ 0 & 0 & 0 & c_{i\to h}(E_{i,n}, E_{h,n}) \end{pmatrix} \tag{4.4}$$

Where the $c_{i\to h}(E_{i,n}, E_{h,n'})$ is defined as Equation 2.13. Analogously is the D Matrix defined comprising of sub matrices of decay yield matrices as following.

$$D = \begin{pmatrix} d_{l\to j} & d_{l\to l} & d_{l\to k} & . & . & . \\ . & . & . & . & & \\ . & . & . & & & \\ d_{k\to j} & d_{k\to l} & d_{k\to k} & . & . & . \end{pmatrix} \tag{4.5}$$

The decay yield matrices have also the same configuration and triangular shape as the interaction yield matrices.The Figure 4.1a and Figure 4.1b depicts the C and D matrices.

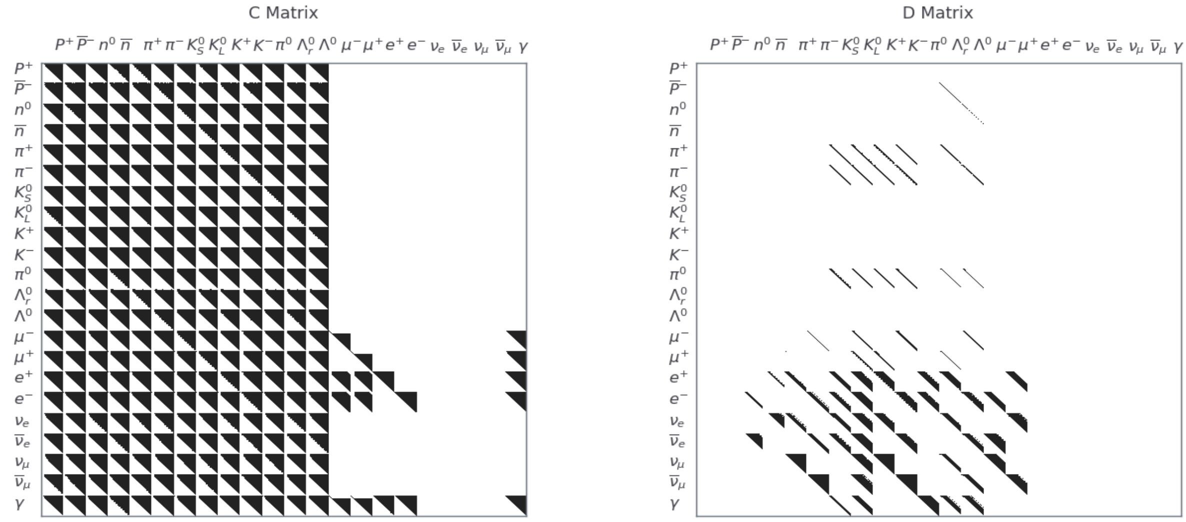

(a) The distribution of C Matrix depicting the triangular shapes of interaction yield matrices

(b) The distribution of D Matrix depicting the triangular shapes of decay yield matrices

Figure 4.1.: The distribution of Cand D matrices

The rows in the Matrices are for every child particles where as a column has the same parent particle. In the similar manner the yield matrices are defined such that a column has the same energy of parent particle where as the row has the same energy of the child particle hence the 'upper' triangular shape.

$$L = \mathbf{diag}(\frac{1}{\lambda_{i,E_1}}, ..., \frac{1}{\lambda_{i,E_n}}, ..., \frac{1}{\lambda_{j,E_1}}, ..., \frac{1}{\lambda_{j,E_n}}, ...) \tag{4.6}$$

As described in Equation 4.6 the inverse of interaction lengths and decay lengths(without the mass density factor included) for various particles over the energy bins are inserted in diagonal places of $L_{int/dec}$ matrices. So far the neutrino oscillations have not been considered to the SACSim. Because of the MSW effect as briefly described in chapter 1 these probabilities would be dependent on the number density of electrons inside the sun at every slant depth. This steps could not be implemented because of the time constraints of this study so far. This is how the matrix form of the coupled cascade equations has been applied in the MCEq which is used in the SACSim being developed. Solving the matrix form of cascade equation we require the initial conditions meaning the initial fluxes, which are in our case cosmic ray influx.

4.1.1. The Primary Model

The cosmic ray influx model is called the 'Primary Model'. There are several primary models available that could be used.

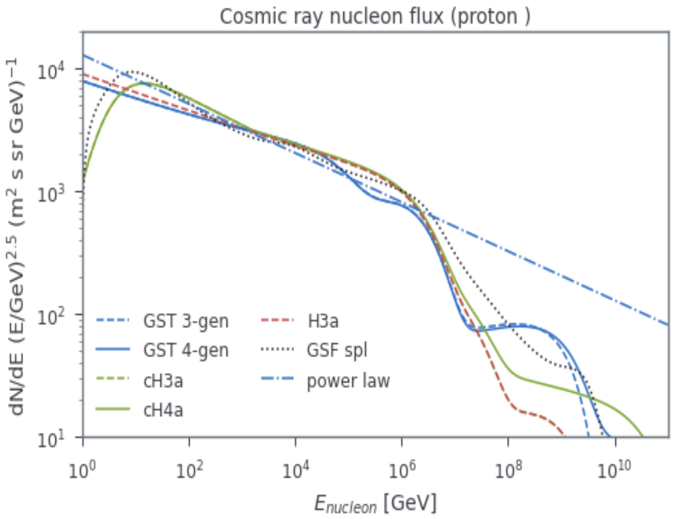

Figure 4.2.: The comparison between several Primary models such as H3a, GST, CH and the power law

In the Figure 4.2 several primary models available have been used to plot cosmic ray flux of proton along with the power law approximation for the cosmic ray flux of proton.

$$\frac{d\Phi_P}{dE} = 1.3 \times 10^4 \times E^{-2.7} \tag{4.7}$$

The power law used in the Equation 4.7 has been used in the study conducted in [26]. The H3a primary model has been used for this study instead of the power law approximation. The primary reason for this is that models developed adjust spectral index of fluxes for various particles depending on the energy range. This helps to simulate the knee and the ankle regions of cosmic ray fluxes. The fluxes from the knee have origins from outside of our solar system(galactic). The knee region is the region in Figure 4.2 approximately between energy range 10^7-10^8 GeV where there is a steep decline in the fluxes. The solar system does not have a stellar object that could accelerate the particles therefore they are thought to be galactic in origin. At the same time the fluxes from ankle region are thought to be originated from outside of our galaxy(extra galactic). The ankle region is the region from approximately 10^7 to 10^9 GeV where the fluxes are declining slowly in compare to the knee region. As discussed in chapter 2 the paths of the cosmic rays are affected by the external magnetic fields. Since the external magnetic fields are not symmetric throughout the space the cosmic rays gets deflected. The degree of deflection is inversely proportional to the energy of the cosmic ray particles. Therefore the relatively low energy particle originating from outside of our solar system are absent from the cosmic ray influx observed at earth.Therefor in the above mentioned regions the galactic and extra galactic sources dominate.

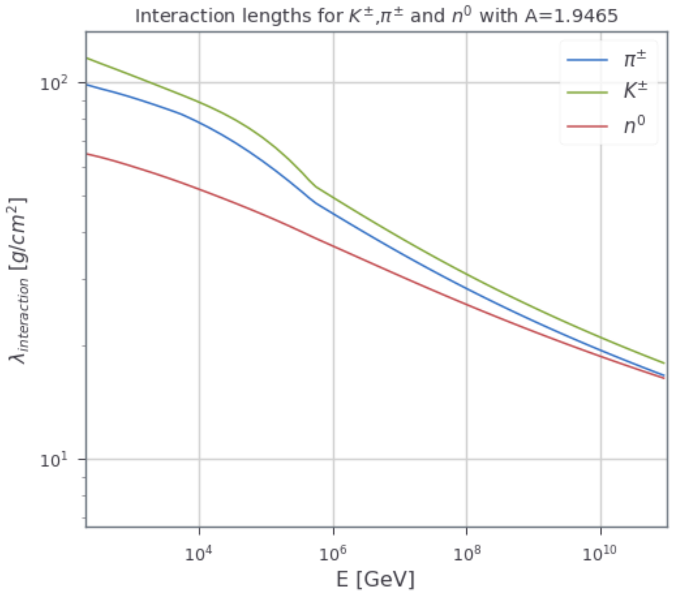

Figure 4.3.: The interaction lengths for the $\pi^{\pm}$, $K^{\pm}$ and n^0 with average mass number for sun A=1.9465 with the total inelastic cross sections for the collisions between the particle in focus and proton as per the parameterization of the Equation 2.8.

4.1.2. The Interaction Model

The interaction models are the back bone of the SACSim or any such simulation models because they describe the yield matrices for the various interaction channels. MCEq has also various models available such as SIBYLL 2.3, SIBYLL2.3cpp, EPOS-LHC, QGSJet. The main difference amongst them would be for what process they are primarily defined. For example as described also in chapter 2 the SIBYLL 2.3 is defined for the cosmic ray earth air shower where as the EPOS-LHC is developed for minimum bias hadronic interactions, used for both heavy ion interactions and cosmic ray air shower simulations [27]. The SIBYLL 2.3 cpp is developed for PP collisions and as discussed in chapter 2 has been used for this study focusing mainly the range of energy above 200 GeV. The interaction models provide the interaction yield matrices as well as the total inelastic cross section for various interaction channels which in turn are used not only to construct the C matrix but also to extract the interaction length via the Equation 2.10 with A=1.9465 as described in chapter 2. The Figure 4.3 has been plotted with the use of SIBYLL 2.3 cpp interaction model and the Equation 2.8 with the A=1.9465 for the sun. The inelastic cross sections given by SIBYLL2.3cpp are for the collision between the particle in focus and the proton. The parameterization described in the Equation 2.9 is used to modify the system for the atmosphere of the sun.

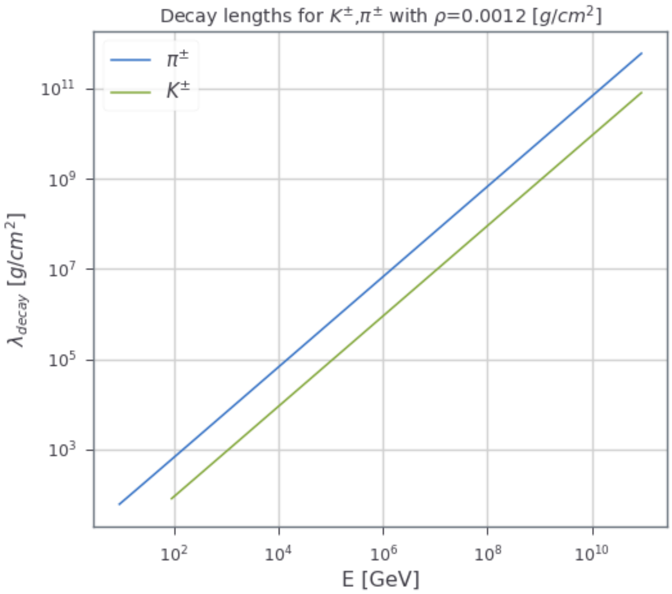

Figure 4.4.: The decay lengths for the $\pi^{\pm}$ and $K^{\pm}$ for the mass density of 0.0012 g/cm^2.

4.1.3. The Decays

The decays are not dependent on the interaction model chosen. The MCEq provides the decay yield matrices and are used to construct the D matrix. The decay lengths are calculated in a different manner in MCEq. The eigenvalues of decay yield matrices of the particles are the decay lengths for various channels as the author describes in the ref [25]. The inverse of these decay lengths can be added and the inverse of that summation is then the total decay length of the parent particle in focus. The Figure 4.4 has been drawn with the decay lengths provided by the MCEq which do not have mass density factor inherently which allows user to modify the medium. The mass density used in the Figure 4.4 is 0.0012 g/cm^2 .

4.2. The Solar Model

The solar model is computer simulation of the sun. The sun is massive with radius 6.957×10^{10} cm. As described in chapter 3, in order to simulate the fluxes, the paths for cascades are parameterized to the shortest distance achieved for any particular paths with respect to the centre of the sun. The density profile derived from model-S is given with respect to the parameter r=R/R_{sun} , where as for the Equation 2.5 the density dependent on the slant depth X is needed ,therefore first the calculation of the slant depth with the Equation 2.6 is carried out for the density profile. The slant depth resulted is for the cascade traveling towards the centre entering perpendicular to the surface of the sun. For the case of the path as described in chapter 3 of cascade, the distance l would be parameterized with the trigonometric formulas in impact parameter b and the local radius R. For data set of local radius R, the shortest

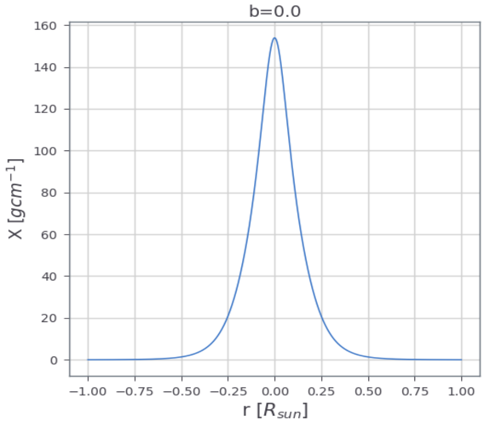

(a) b=0

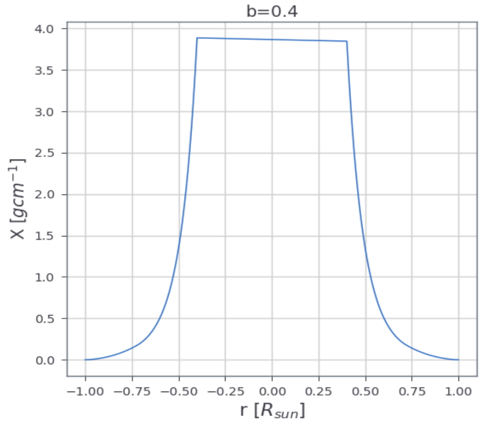

(b) b=0.4

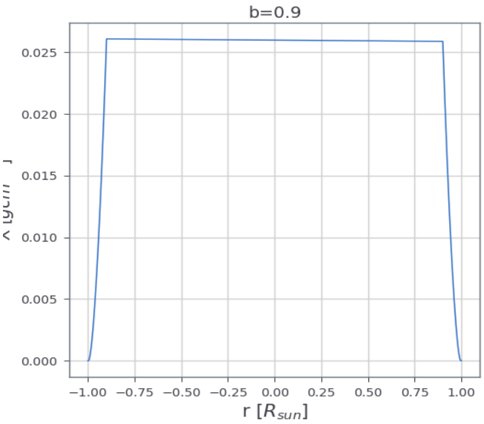

(c) b=0.9

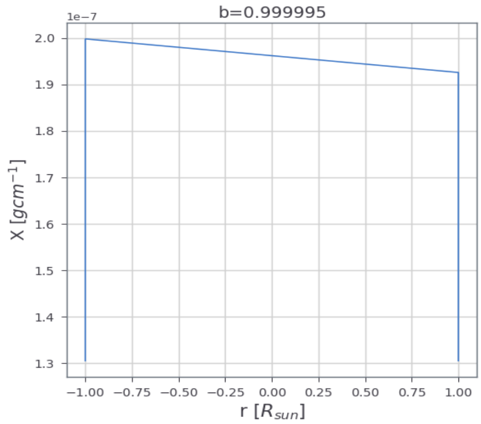

(d) b=0.999995

Figure 4.5.: The density depending on local radii for various impact parameter b

distance from the centre of the sun achieved for the path in focus i.e impact parameter b*R_{sun} is calculated and the data set is then taken from the surface of the sun up until this shortest radius.

The data set is then mirrored and added to the original data set of radius. As Figure 4.5 depicts for different impact parameter b, the shortest local radius achieved changes the maximum density achieved. The negative r meaning the second quadrant from where the path is starting from. Now the data set for the radii achieved from this modification is then applied to the trigonometric formula in order to achieve data set for the distance traveled and this path length data is then interpolated with the modified data of the local densities.

$$X_b = \int_0^L \rho(l_b(r))dl_b(r) \tag{4.8}$$

These interpolation of mass densities to the path length helps to simulate the Equation 4.8

Where L is the total length traveled along the path. This simulation results in the slant depth data set as depicted in the Figure 4.6 for various impact parameter b. The slant depth data set then is interpolated to the mass density data set, therefore giving us a set of interpolation function $\rho_b(X)$. This will be used for solving the coupled cascade equations.

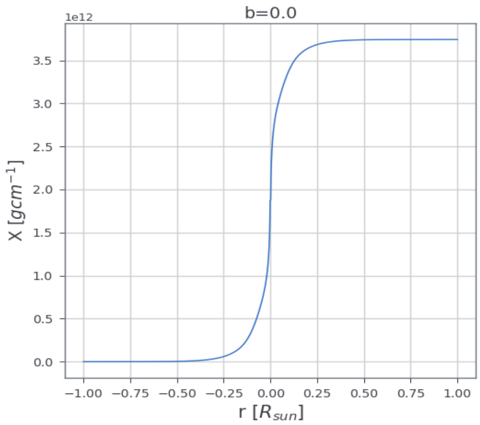

(a) b=0

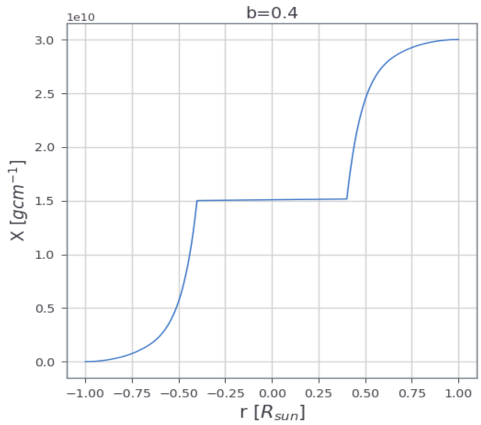

(b) b=0.4

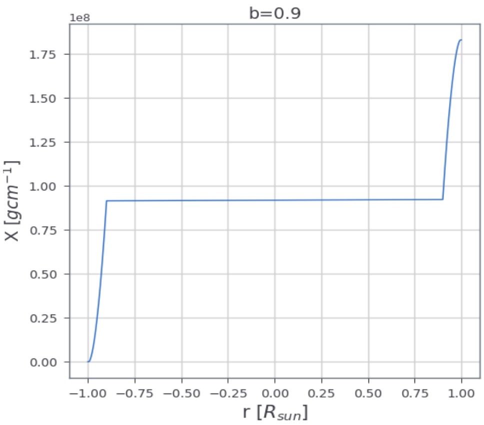

(c) b=0.9

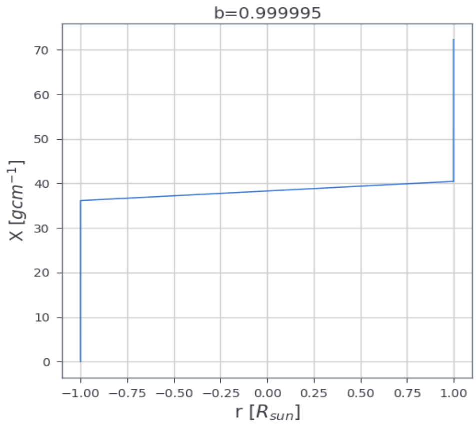

(d) b=0.999995

Figure 4.6.: The density depending on local radii for various impact parameter b

4.3. The ODE Solver

The ODE solvers (Ordinary Differential Equation solvers) are the functions or methods, as name suggests, to solve numerically the ordinary differential equations. These numerical methods are provided by various libraries of python such as SCIPY or they could be developed manually. These are initial value problem (IVP) solvers i.e. the problems with known initial conditions . The initial conditions for the case of the cascade equations are the cosmic ray fluxes from the primary model 'H3a'. There are three types of ODE solvers

- **Explicit Method**: Explicit methods calculate the state of the system at a later time from the state of the system at the current time without the need to solve algebraic equations, In the case of Cascade equations the variable is slant depth X. e.g. Forward Euler method, Adams–Bashforth methods, Runge-Kutta methods etc.

- **Implicit Method**: Implicit methods find a solution by solving an equation involving both the current state of the system and the later one. e.g. backward Euler method, implicit Runge-Kutta methods, Adams-Moulton methods etc.

- **Mixed Explicit-Implicit Method**: Mixed explicit-implicit Method, as name suggests, makes use of both implicit and explicit methods i.e it switches between the methods according to the stiffness of the differential equation. e.g Crank Nicolson method, forward-backward Euler method, LSODA etc.

The stiffness of the differential equation depends on how stable are the numerical methods while solving the differential equation. The step-size is how long of a jump could be taken in the variable i.e time or slant depth so that the solution does not loose accuracy. In order for a numerical method to give a reliable solution to the differential system, sometimes the step size is required to be at infinitely small level in a region where the solution curve is very smooth. The phenomenon is known as stiffness [28].

The implicit methods tend to converge i.e they are stable whereas the explicit methods are not but the implicit methods are not always accurate. The explicit methods are faster in nature on the other hand the implicit methods are slower nature but stable. A simple example is given in appendix A.1 where comparison between common methods has been performed and a detailed description on this topic could be found in [28]. This is why depending on the nature of differential equations the methods are chosen. This requires a balance between the stability of the solver and the step-size required as well as the accuracy of the solution. The mixed explicit-implicit methods are a better option, when the nature of the differential equation is unknown because of its smart switching between the methods, the accuracy is also maintained as well as the computational power could be also limited. Therefor in SACSim method 'LSODA' is used written by Linda R. Petzold and Alan C. Hindmarsh. This method is written as FORTRAN ODE and there are several functions provided by various libraries of python to implement this method in a python code. In the SACSim scipy library has been used because of its universality. There are two such functions '*odeint*' and '*solve_ivp*' provided in

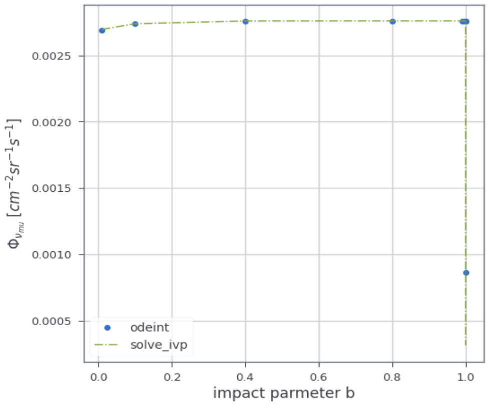

(a) Comparison in b=0 to 1

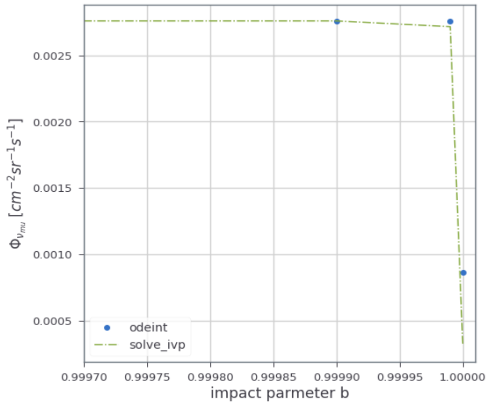

(b) Comparison in b= 0.9997 to 1.0001

Figure 4.7.: Comparison of the final fluxes of v_{mu} calculated from *odeint* and *solve_ivp* functions

scipy library. The *odeint* solver stores the solutions at every data point of variable, slant depth X dataset, whereas *solve_ivp* with method 'LSODA' stores the solution at limited number data points. The *solve_ivp* in this manner is faster than the *odeint* solver. As depicted in the Figure 4.7 the total fluxes at various impact parameters with the help of both solvers *odeint* and *solve_ivp* has been calculated . These fluxes are for the entire energy range available in MCEq i.e from 0.089 GeV to 8.9×10^{10} GeV. From the Figure 4.7a it could be concluded that the both solver reproduce similar results for the range of impact parameter b=0 to 0.999. The Figure 4.7b is a magnified version of the Figure 4.7a for range 0.997 to 1.0001. This reveals that there is a variation in the results in this region.

As could be concluded from the Figure 4.8a the difference between the results increases rapidly as impact parameter b increase. This is due to the larger step-size the *solve_ivp* method takes which does not affect the results for lower impact parameter where the cosmic rays have to travel through the sun significantly but affects significantly for impact region near the surface(i.e b=0.9 to 1). Therefore the *odeint* method is more useful and precise in order to analyse the fluxes near the surface impact region as well as to analyse how the fluxes change throughout the flight path inside the sun because of its ability to store the solution for specified data points. Whereas the *solve_ivp* is more useful for achieving approximate results for impact parameter b= 0 to about 0.99 . Although as Figure 4.8b depicts, the percentage difference in results is negative i.e the fluxes are lower in comparison to the the fluxes from *odeint* with the same reasoning of step-sizes being larger. At the same time the percentage differences are lower than 0.1 which could be neglected for this impact region in order to minimize the computational time required because the *solve_ivp* takes approximately 2/3 amount of time as compared to *odeint* which makes a difference for large calculations.

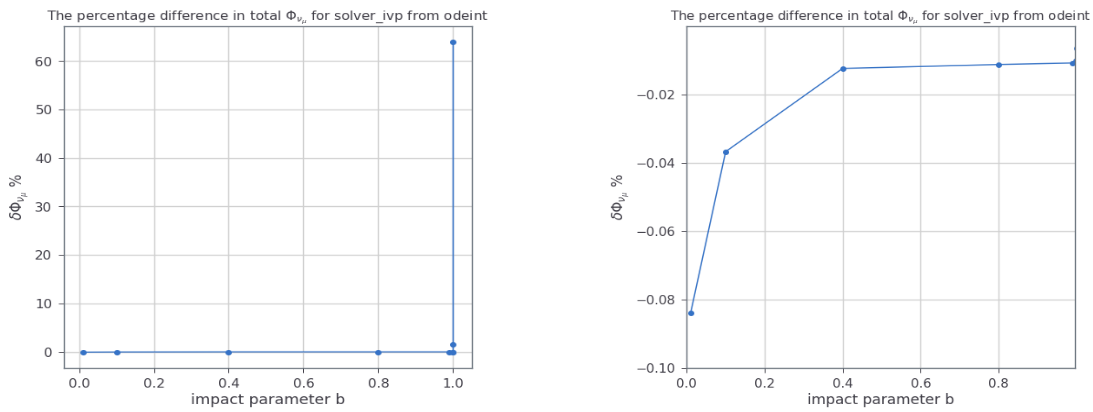

(a) Comparison in b=0 to 1

(b) Comparison in b= 0 to 0.9

Figure 4.8.: The percentage deviation of Φ_{ν_μ} calculated by *odeint* to the results calculated by *solve_ivp*. The deviation increases significantly impact region near surface as impact parameter is increased.

4.4. Analysis and Results

The SACSim is now ready to use for calculating solar atmospheric neutrino fluxes for various impact parameters with primary model "H3a" and interaction model "SIBYLL2.3cpp". The SACSim developed takes about 5000 seconds to calculate fluxes for the 22 cascade particles considered with the configuration of computer being intel i5-6th generation,8gb DDR3 RAM, 512 gb SSD.

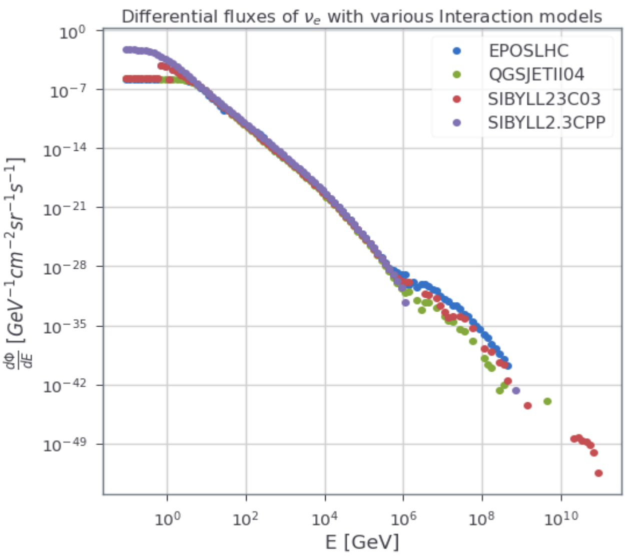

Figure 4.9.: Differential fluxes of ν_e with various interaction models at b=0.8. The fluxes depict minimal deviations regardless of interaction models

The Figure 4.9 depicts the differential fluxes with respect to the E_ν at impact parameter b=0.8. The fluxes are comparable to each other and the deviations are minimal regardless of the interaction model. The parameterization as depicted in Equation 2.9 to normalize the total cross sections has been used.

The Figure 4.10 describe the change in differential fluxes with respect to the parameter r=R/R_{sun} of ν_μ, ν_e for three different energies of particle in focus at impact parameter b=0. As it could be concluded from the Figure 4.10 that the production of these particles is majorly concentrated near the surface as they enter the sun. Between the parameter r=1.0005 to 0.9995 the production peaks and declines and for rest of the sun it remains constant. The negative sign of parameter r is because the cosmic rays are entering from the second quadrant and traveling through the sun as the centre of the sun is thought to be the origin point. The production curve is shifted towards left when compared to the production curves observed in the [20]. This is because of variation in SSM used for the both studies.

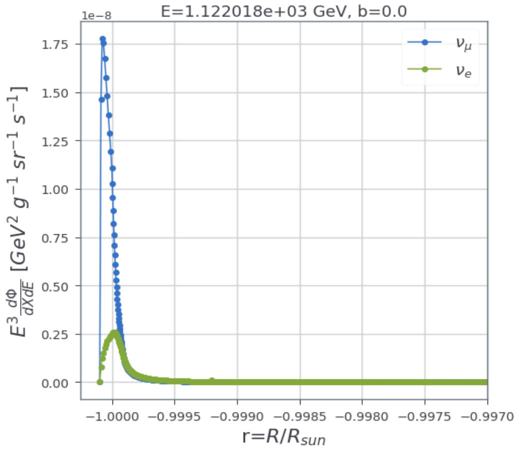

(a) E=1122 GeV

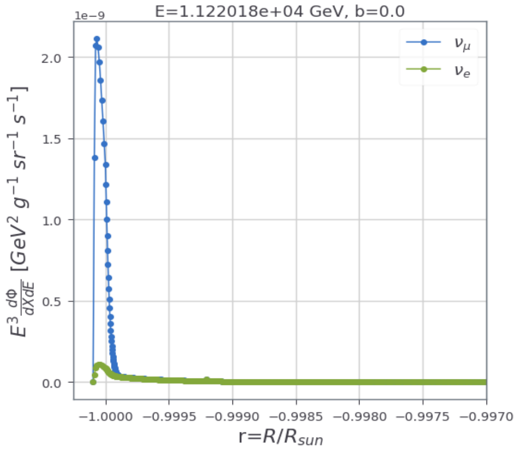

(b) E=11220 GeV

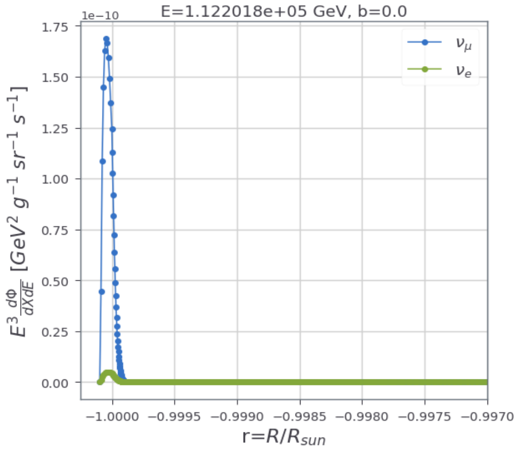

(c) E=112201 GeV

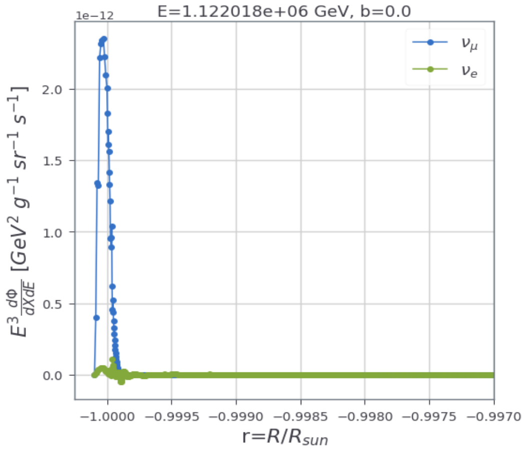

(d) E=1122018 GeV

Figure 4.10.: Production curve: The change in differential fluxes depending on the primary energy with respect to the local radii for ν_e,ν_μ with impact parameter b=0.

As the energy of neutrinos in focus increases the primary energy required to produce these neutrinos also increases for which the primary fluxes i.e the cosmic ray influxes are lower resulting in lower production. The peak of production near the surface showcases that the total fluxes produced after cosmic ray particles have passed through the sun for various impact point which are lower than 0.99 would not have major differences. This is because most of the production happens at the similar region of their paths. This could be confirmed from Figure 4.7a where the total fluxes for various impact parameters have been plotted. The slight decrease in total fluxes between b=0 to 0.1 is because of neutrino attenuation. The neutrino attenuation i.e the neutrino interactions via weak channels with the sun. This effect could be observed there majorly, that is because of the high density near the centre of the sun. This effect is seen depleting with the rapid fall in density as impact parameter increases. The fall in fluxes for impact region closer to surface that is b=0.99 to 1.00 deplete rapidly which is trivial because of the rapid fall in density. This also means that compared to lower impact parameter the other particles present in the cascade after traveling through the path would be higher. The fluxes of other particles such as $\mu^{\pm}$ are significantly low as depicted in Figure 4.11 for various impact parameters. But this changes for impact region near the surface, where there is not enough material for interactions to take place. This results in heightened fluxes for heavier particles than neutrinos and lower differential fluxes of neutrinos. The Figure 4.11 depicts this phenomenon as Figure 4.11a has higher neutrino differential fluxes where as lower differential fluxes of heavier particles such as Λ^0,$\mu^{\pm}$ compared to the differential fluxes shown in Figure 4.11b. Therefore the cascade for near surface impact region has particle fluxes that are not easily negligible. Since after traveling through the sun the particles need to propagate through the vacuum these particles could be thought to decay for more accurate results for the fluxes reaching the earth.

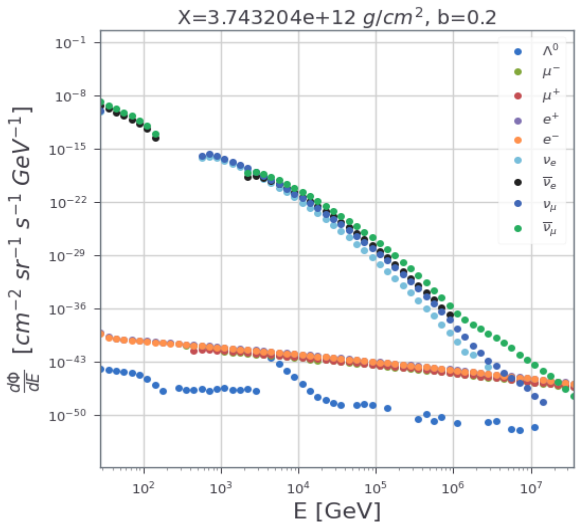

(a) impact parameter b=0.2

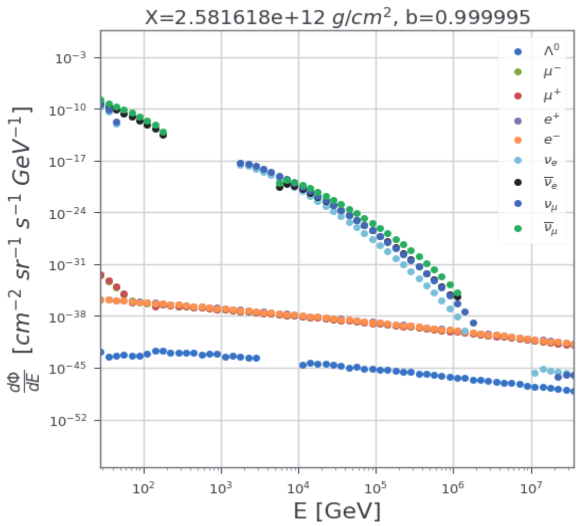

(b) impact parameter b= 0.999995

Figure 4.11.: Differential fluxes at impact parameter b=0.2 and 0.999995 with respect E_{sec}

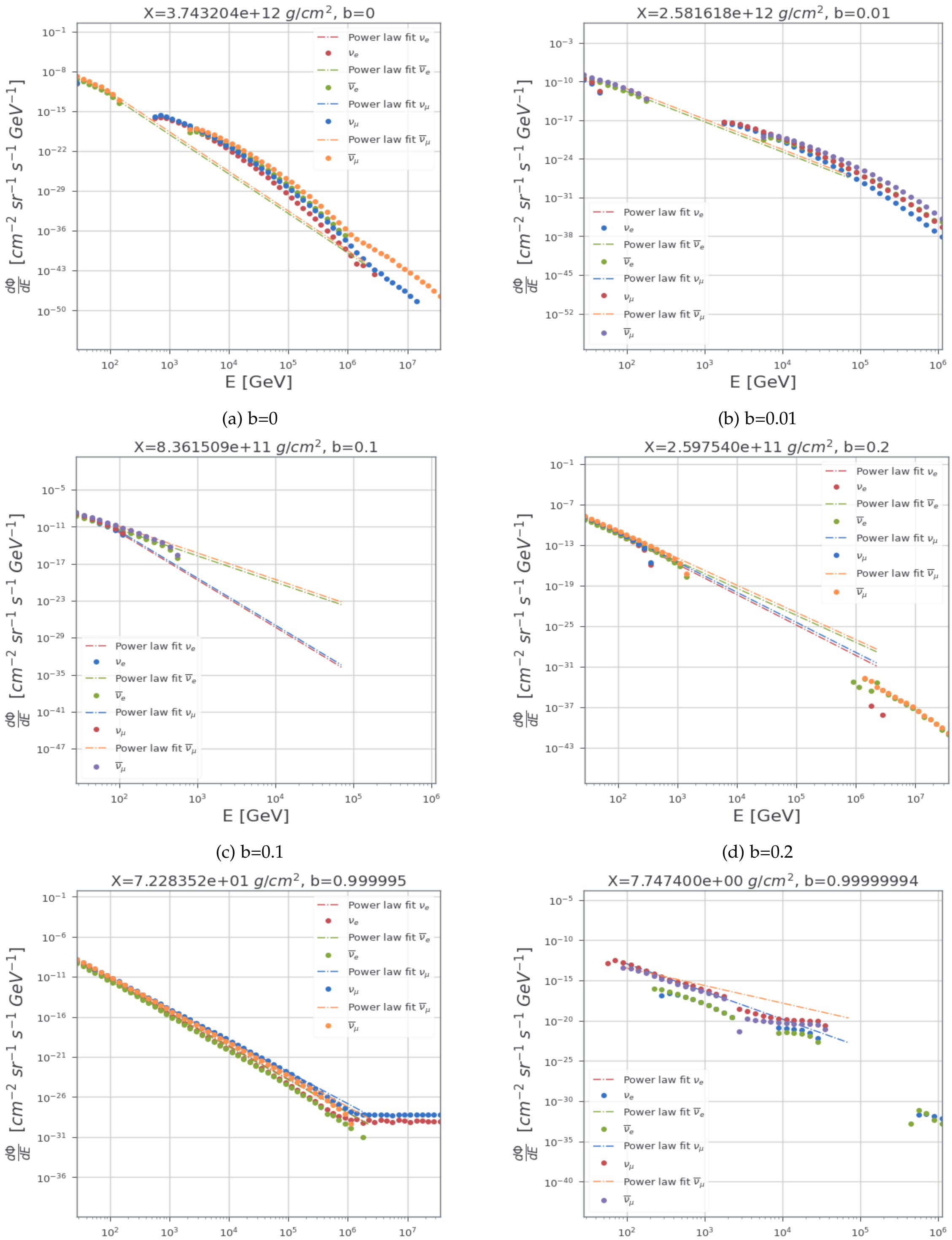

(a) b=0

(b) b=0.01

(c) b=0.1

(d) b=0.2

(e) b=0.999995

(f) b=0.99999994

Figure 4.12.: Differential fluxes at various impact parameter b for ν_e,ν_μ,$\overline{\nu}_e$,$\overline{\nu}_\mu$. The fitting curves have been plotted with the energy spectrum that the differential fluxes follow between energy range of 89 GeV to 89125 GeV. The differential fluxes do not follow the same spectral index above this energy range.

The Figure 4.12 shows the differential fluxes with respect to the E_ν for various impact parameter. The fitting has been done with the power law approximation as Equation 2.3 for the energy range 100 GeV to 10^7 GeV. As could be concluded from these curves that the differential fluxes follow a spectrum index up until a certain energy level after which the curves begin to steepen and the spectrum index increases. The Figure 4.12a and Figure 4.12b have in the higher energy region fluxes for the neutrinos which are absent from the Figure 4.12c depicting an instability in this region of the code, further on as impact parameter increases the fluxes follow a similar pattern up till the b=0.99999994 is reached where the X=7.74 [g/cm^2]. Depicting after this impact parameter the production of neutrinos should be minimal but in that region also there seem to be some instability. These instabilities could be also seen in the spectral index that the differential fluxes follow for the energy range 89 GeV to 2.18 PeV in Figure 4.13. In the Figure 4.13 the power law approximation for spectral index has been used in the energy range mentioned above. From the Figure 4.12 it could be concluded that the differential fluxes do not follow a constant energy spectrum through the energy range also this is because of the neutrino attenuation for high energy region as well as the primary fluxes do not follow a constant spectrum index as the spectrum is adjusted through out the energy range depending on the dominating source.

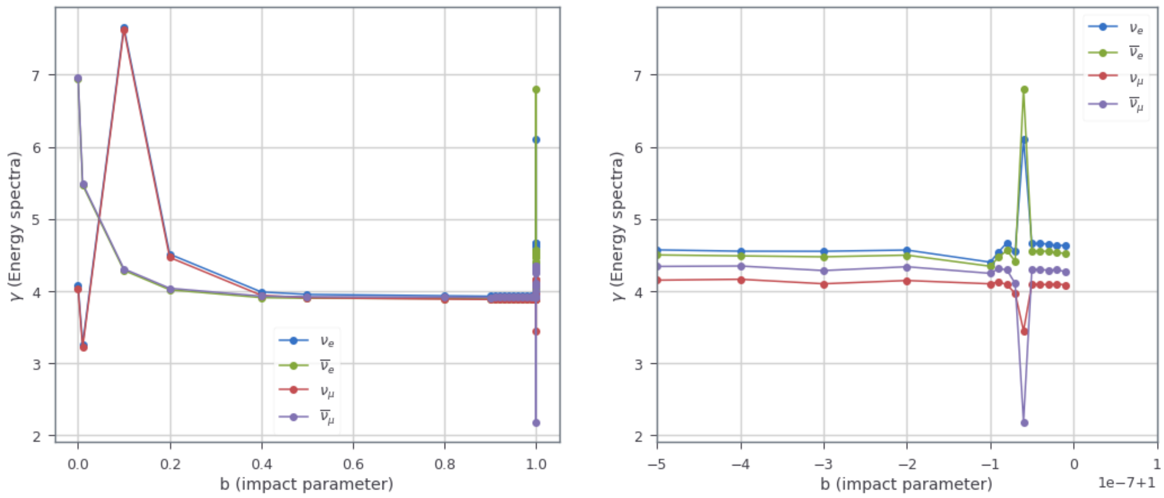

(a) impact parameter b=0 to 1.00

(b) impact parameter b= 0.999 to 1.0

Figure 4.13.: Energy spectra γ vs impact parameter b: The energy spectra changes as the impact parameter changes. Increase in the energy spectra implies that the fluxes are decreased which could be seen for the impact regions near the center and near surface.

The spectrum index also varies with respect to the impact parameter as could be concluded from Figure 4.13. The high spectrum index implies lower differential fluxes . This higher values of spectrum index in impact region close to the core is due to neutrino attenuation as discussed before seen in Figure 4.13a , whereas the approximately constant spectrum index is the result of approximately same production curves in the rest of the region. The peak seen in Figure 4.13a near b= 0.1 and the peak in Figure 4.13b depict the expected behaviour of differential fluxes dropping down for these regions, whereas the spectrum indices in the left of the peak at b=0.1 and the indices in the right of peak near b=0.99999994 backs the instability mentioned above. Both of the peak seen here are the result of lower productions , The reasoning behind the first peak is the neutrino attenuation happening in the core region where the mass density is very high on the other hand the peak in impact region near the surface is a result of fewer interactions taking place due to the lack of material. These both phenomenon can be also seen in the Figure 4.14a and Figure 4.14b where for the above mentioned impact parameters a steep decline could be observed.

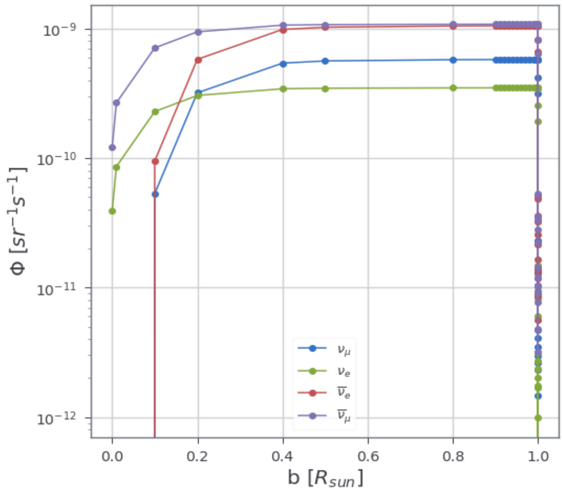

(a) impact parameter b=0 to 1.00

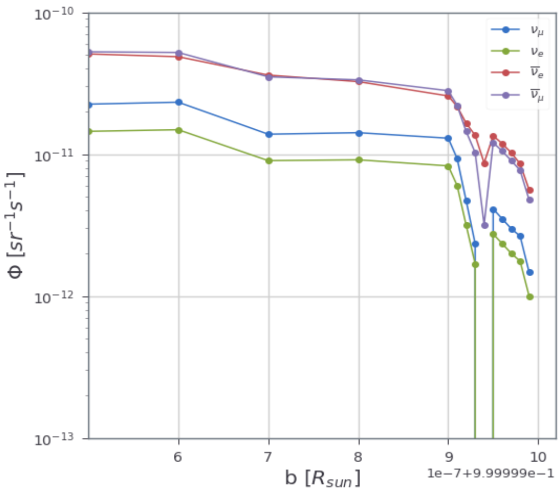

(b) impact parameter b= 0.999 to 1.0

Figure 4.14.: Total flux Φ vs impact parameter b: The total fluxes follow a constant value for the impact parameter b=0.2 to 0.999995. The neutrino interactions and insufficient interactions are the cause of the steep decline in the fluxes for impact parameters 0.1 and 0.99999994.

The Figure 4.14a implies that the total fluxes follow almost constant value for impact parameter b=0.2 to 0.999995. This is due to the production region being near the surface as could be seen in Figure 4.10. This is why the effect of neutrino attenuation is more visible where the densities are high.

The total fluxes(integrated over energy bins) could be approximated and taken as an average over a ring having radius depending on the impact parameter. As discussed above the total fluxes over impact parameter b=0.2 to 0.9 remain almost constant therefore in that region the ring radii could be taken in bigger intervals. The ring radii can be calculated from angular profile. The angular profile for the sun is obtained from Equation 3.6 , R_{sun} and R_{orbit}. These integrated fluxes now are multiplied with the ring perimeter and the radii interval, thus resulting in the total fluxes with units $sr^{-1}s^{-1}$. These fluxes are then added up to achieve the total number of neutrino per second. These total fluxes (s^{-1}) along with the neutrino oscillations in vacuum can be estimated for the scenario of them reaching the earth. The approximation mentioned in subsection 2.2.3 for the earth-sun distance could be used here with the probabilities given in Equation 1.16-Equation 1.20 for the case of vacuum oscillations to estimate the flux of neutrinos reaching the earth.

Particle	$\Phi_{sun}[\ s^{-1}]\times 10^{13}$	$\Phi_{earth}[\ s^{-1}]\times 10^{12}$
ν_e	0.83	8.26
ν_μ	1.50	7.59
ν_τ	0	7.44

(a) Low energy cutoff at 89 GeV

$\Phi_{sun}[\ s^{-1}]\times 10^{10}$	$\Phi_{earth}[\ s^{-1}]\times 10^{9}$
0.86	8.96
1.72	8.46
0	8.32

(b) Low energy cutoff at 891 GeV

Table 4.1.: The total fluxesΦ [s^{-1}] after production at sun and the total fluxes reaching the earth after oscillation in vacuum with $\sin^2\theta_{23}$=0.45$(1^{+0.35}_{-0.20})$ with normal hierarchy

In the Table 4.1 the final fluxes are given after production in the sun and fluxes at the earth. The ratio for ν_μ and ν_e fluxes is in deficit than the 1:1 which is in accordance with the observed fluxes. The $\sin^2\theta_{23}$ has been taken $0.45(1^{+0.35}_{-0.20})$ with normal hierarchy. The uncertainty in the results depend on accuracy of the oscillation parameter as well as accuracy of interaction, primary and solar models.

5. Conclusion

In conclusion the simulation model developed is a flexible tool to apply for a wide variety of scenarios. SACSim allows to analyse the fluxes from various impact parameter for wide range of particles and due to its flexibility, further particles and their interaction-decay channels could be added with an ease providing more degree of freedom.

In this study, analysis have been done for the differential fluxes at various impact parameters. The effects of density on these fluxes have been also explored as well as the accuracy of SACSim have been also looked upon. The study done in [29] where seven years of data have been analysed have not found an experimental observation of SAν but as they expect in future more sensitive experiments such as IceCube Gen-2 or KM3NeT would provide better sensitivity for SAν detection. The upper limit for differential neutrino flux at 1 TeV of 1.02×10^{-13} GeV^{-1} cm^{-2} s^{-1} expected in [29] from [20] model is in close vicinity with the estimation of 1.60×10^{-13} GeV^{-1} cm^{-2} s^{-1} at 0.89 TeV from SACSim. This motivates a new analysis from more data .

The inclusion of energy loss terms and MSW effect in neutrino oscillations for the sun would imply more accurate results. The value of θ_{23} previously estimated approximately $\pi/4$ of case maximal mixing reported in [30] has deviation from this value reported in [31] from experimental data of NOvA (NuMI Off-axis ν_e Appearance). This can also be seen in our study from the table 4.1 where the flux ratio is in accordance with observation of deficit in 1:1 ratio for the case of $\sin^2\theta_{23} = 0.45$. In this manner with more accurate interaction models, Primary models and parameter with better accuracy , SACSim can provide an optimal platform for simulation. The instability issues discussed here are expected to be resolved with the help of accurate models.

The neutrino fluxes obtained by SACSim can provide an estimation of background for studies concerning the dark matter e.g SACSim can be applied for analysis of interactions or annihilation processes in the sun of a certain dark matter candidate. SACSim can be used for simulation of atmospheric cascade from any stellar object with the help of the density profile of that stellar object . This can be also used for exploration and simulation of exo-bodies. SACSim will be made available on open-source platform https://gitlab.lrz.de as soon as possible.

A. Appendix

A.1. ODE solver example

Let us consider a differential equation as Equation A.1 with inital value y_0

$$\frac{dy}{dt} = \lambda f(t) \tag{A.1}$$

The analytical solution of Equation A.1 is as Equation A.2,

$$y = e^{t\lambda f(t)} \tag{A.2}$$

The y_i is the value of y corresponding to the i^{th} step. The forward Euler method is an example of an explicit method.

$$y_i = y_{i-1} + \lambda f(t_{i-1})h \tag{A.3}$$

The eq:explicit describes the solution with the forward Euler method where the h is the step size i.e $x_i - x_{i-1}$. The backward Euler method on the other hand is an example of implicit method.

$$y_{i+1} - y_i = \lambda f(t_{i+1})h \tag{A.4}$$

The Equation A.4 provides the solution with implicit method. The trapezoidal rule is a common example of mixed implicit -explicit method,

$$y_{i+1} = \left(\frac{1 - \frac{h\lambda}{2}}{1 + \frac{h\lambda}{2}} \right)^{i+1} y_0 \tag{A.5}$$

The fig:h depicts that the better accuracy could be achieved by decreasing the step-size but that is not always possible. Moreover the mixed implicit -explicit method provide more reliable solutions even with the increased step size. A more detailed description and derivations of the methods could be found in [28] .

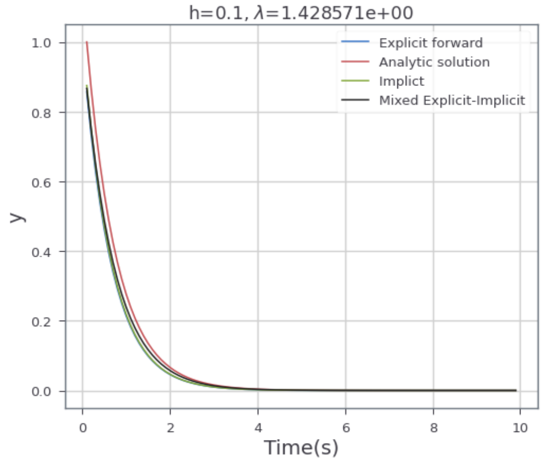

(a) h=0.1

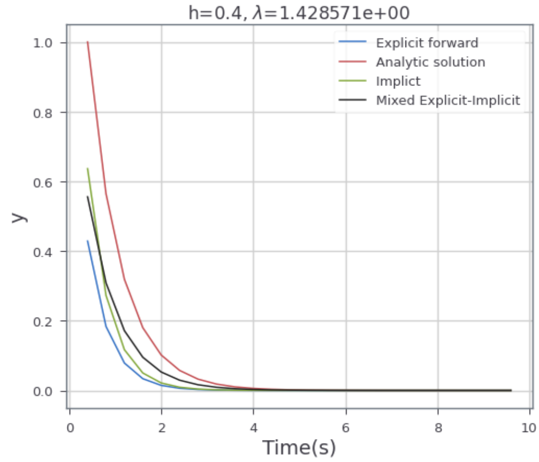

(b) h= 0.4

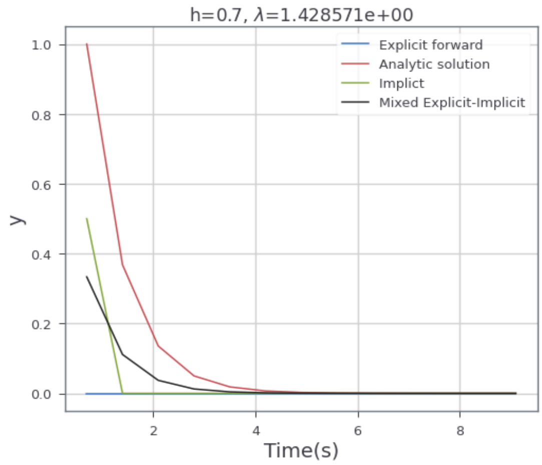

(c) h=0.7

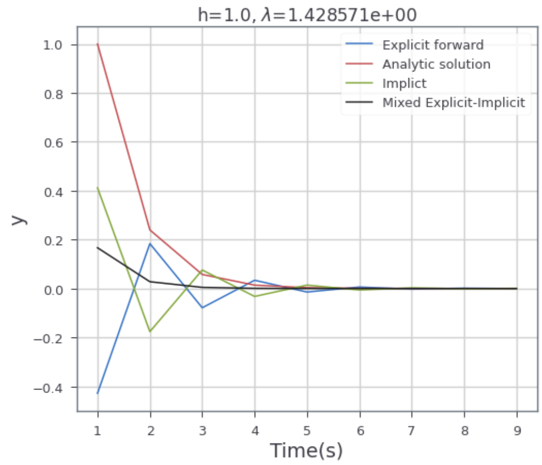

(d) h=1

Figure A.1.: The solutions with various methods with $\lambda \approx 1.43$ at various step-size. As the step sizes increases the accuracy of the solution also decrease.

A.2. Comparison plot between MCEq and SACSim total inelastic cross section of proton

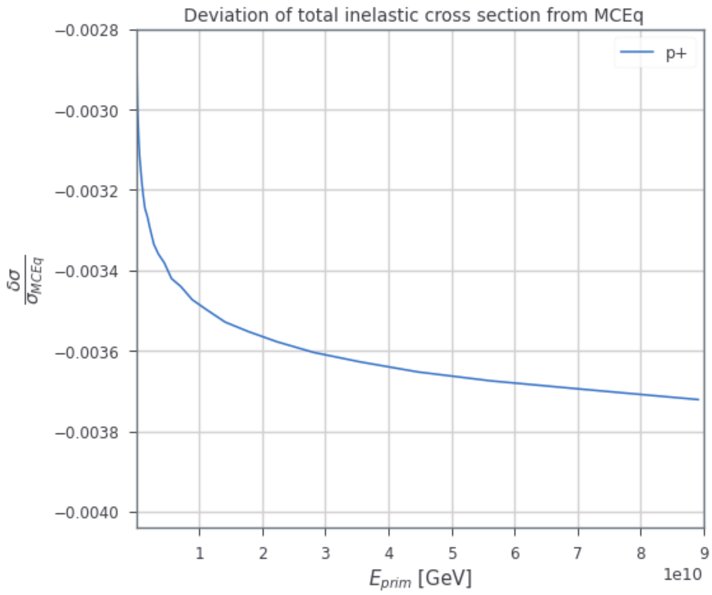

Figure A.2.: Deviation of total cross section between MCEq and SACSim. This depict approximately 0.3% lower values of the total cross section for the SACSim from MCEq

List of Figures

Bibliography

[1] J. Becker Tjus, P. Desiati, N. Döpper, H. Fichtner, J. Kleimann, M. Kroll **and** F. Tenholt. "Cosmic-ray propagation around the Sun: investigating the influence of the solar magnetic field on the cosmic-ray Sun shadow". **in**: *Astronomy Astrophysics* 633 (**january** 2020), A83. ISSN: 1432-0746. DOI: `10.1051/0004-6361/201936306`. URL: `http://dx.doi.org/10.1051/0004-6361/201936306`.

[2] J. Christensen-Dalsgaard, W. Dappen, S. Ayukov, E. Anderson, H. Antia, S. Basu, V. Baturin, G. Berthomieu, B. Chaboyer, S. Chitre, A. Cox, P. Demarque, J. Donatowicz, W. Dziembowski, M. Gabriel, D. Gough, D. Guenther, J. Guzik, J. Harvey **and** R. Ulrich. "The Current State of Solar Modeling". **in**: *Science (New York, N.Y.)* 272 (**june** 1996), **pages** 1286–92. DOI: `10.1126/science.272.5266.1286`. URL: `https://users-phys.au.dk/jcd/solar_models/`.

[3] M. Ahlers, K. Helbing **and** C. Pérez de los Heros. "Probing particle physics with IceCube". **in**: *The European Physical Journal C* 78.11 (**november** 2018). ISSN: 1434-6052. DOI: `10.1140/epjc/s10052-018-6369-9`. URL: `http://dx.doi.org/10.1140/epjc/s10052-018-6369-9`.

[4] "The Detection of Neutrinos in IceCube". **in**: (). URL: `https://masterclass.icecube.wisc.edu/en/learn/detecting-neutrinos`.

[5] A. Ioannisian **and** S. Pokorski. "Three neutrino oscillations in matter". **in**: *Physics Letters B* 782 (**july** 2018), **pages** 641–645. ISSN: 0370-2693. DOI: `10.1016/j.physletb.2018.06.001`. URL: `http://dx.doi.org/10.1016/j.physletb.2018.06.001`.

[6] A. Das. "V-A theory: A view from the outside". **in**: (2009).

[7] C. Giunti **and** C. W. Kim. "Fundamentals of neutrino physics and astrophysics". **in**: ProQuest Ebook Central, 2007. URL: `https://ebookcentral-proquest-com.eaccess.ub.tum.de`.

[8] G. L. Fogli, E. Lisi, A. Mirizzi, D. Montanino **and** P. D. Serpico. "Oscillations of solar atmosphere neutrinos". **in**: *Physical Review D* 74.9 (**november** 2006). ISSN: 1550-2368. DOI: `10.1103/physrevd.74.093004`. URL: `http://dx.doi.org/10.1103/PhysRevD.74.093004`.

[9] T. K. Gaisser, R. Engel **and** E. Resconi. "Cosmic rays". **in**: *Cosmic Rays and Particle Physics*. 2 **edition**. Cambridge University Press, 2016, **pages** 1–11. DOI: `10.1017/CBO9781139192194.003`.

[10] C. P. et al. (Particle Data Group). *Cosmic rays*. Chin. Phys. C, 40, 100001, 2016.

[11] D. Seckel, T. Stanev **and** T. K. Gaisser. "Signatures of Cosmic-Ray Interactions on the Solar Surface". **in**: 382 (**december** 1991). Provided by the SAO/NASA Astrophysics Data System, **page** 652. DOI: `10.1086/170753`. URL: `https://ui.adsabs.harvard.edu/abs/1991ApJ...382..652S`.

[12] K. O'Brien. "The Physics of Electromagnetic Cascade". **in**: *Computer Techniques in Radiation Transport and Dosimetry*. **byeditor**W. R. Nelson **and** T. M. Jenkins. Boston, MA: Springer US, 1980, **pages** 141–171. ISBN: 978-1-4684-3608-2. DOI: `10.1007/978-1-4684-3608-2_11`. URL: `https://doi.org/10.1007/978-1-4684-3608-2_11`.

[13] A. Zilles. *Emission of Radio Waves in Particle Showers*. Springer, Cham, **august** 2017. DOI: `https://doi-org.eaccess.ub.tum.de/10.1007/978-3-319-63411-1`.

[14] M. Asplund, N. Grevesse, A. J. Sauval **and** P. Scott. "The Chemical Composition of the Sun". **in**: *Annual Review of Astronomy and Astrophysics* 47.1 (**september** 2009), **pages** 481–522. ISSN: 1545-4282. DOI: `10.1146/annurev.astro.46.060407.145222`. URL: `http://dx.doi.org/10.1146/annurev.astro.46.060407.145222`.

[15] W. Frass. "Passage od Particles Through Matter". **in**: (2009).

[16] A. Fedynitch, F. Riehn, R. Engel, T. K. Gaisser **and** T. Stanev. "Hadronic interaction model sibyll 2.3c and inclusive lepton fluxes". **in**: *Physical Review D* 100.10 (**november** 2019). ISSN: 2470-0029. DOI: `10.1103/physrevd.100.103018`. URL: `http://dx.doi.org/10.1103/PhysRevD.100.103018`.

[17] "Data files and plots of cross-sections and related quantities in the 2008 Review of Particle Physics". **in**: *Physical Review D* (2008).

[18] W. L. et. al. "ENERGY LOSS OF MUONS IN THE ENERGY RANGE 1-10000 GeV". **in**: (1985).

[19] M. T. et. al. (Particle Data Group). "Passage of Particles Through Matter". **in**: (2018).

[20] J. Edsjö, J. Elevant, R. Enberg **and** C. Niblaeus. "Neutrinos from cosmic ray interactions in the Sun". **in**: *Journal of Cosmology and Astroparticle Physics* 2017.06 (**june** 2017), **pages** 033–033. ISSN: 1475-7516. DOI: `10.1088/1475-7516/2017/06/033`. URL: `http://dx.doi.org/10.1088/1475-7516/2017/06/033`.

[21] S. Degl'Innocenti. "Stellar evolution and the Standard Solar Model". **in**: *EPJ Web of Conferences* 227 (**january** 2020), **page** 01004. DOI: `10.1051/epjconf/202022701004`.

[22] M. K. et al. *SOLAR OPACITY CALCULATIONS USING THE SUPER-TRANSITION-ARRAY METHOD*. ApJ 821 45, 2016.

[23] A. M. Serenelli, S. Basu, J. W. Ferguson **and** M. Asplund. "NEW SOLAR COMPOSITION: THE PROBLEM WITH SOLAR MODELS REVISITED". **in**: *The Astrophysical Journal* 705.2 (**october** 2009), **pages** L123–L127. ISSN: 1538-4357. DOI: `10.1088/0004-637x/705/2/l123`. URL: `http://dx.doi.org/10.1088/0004-637X/705/2/L123`.

[24] R. F. Stein **and** Å. Nordlund. "Simulations of Solar Granulation. I. General Properties". **in**: 499.2 (**may** 1998), **pages** 914–933. DOI: `10.1086/305678`.

[25] A. Fedynitch, R. Engel, T. K. Gaisser, F. Riehn **and** T. Stanev. *Calculation of conventional and prompt lepton fluxes at very high energy*. 2015. arXiv: 1503.00544 [hep-ph].

[26] M. Masip. "High energy neutrinos from the sun". **in**: *Astroparticle Physics* 97 (**january** 2018), **pages** 63–68. ISSN: 0927-6505. DOI: 10.1016/j.astropartphys.2017.11.003. URL: http://dx.doi.org/10.1016/j.astropartphys.2017.11.003.

[27] T. Pierog, I. Karpenko, J. M. Katzy, E. Yatsenko **and** K. Werner. "EPOS LHC: Test of collective hadronization with data measured at the CERN Large Hadron Collider". **in**: *Physical Review C* 92.3 (**september** 2015). ISSN: 1089-490X. DOI: 10.1103/physrevc.92.034906. URL: http://dx.doi.org/10.1103/PhysRevC.92.034906.

[28] M. E. Davis. "Initlal Value Problems for Ordinary Differential Equations". **in**: *Numerical methods and modeling for chemical engineers*. New York : Wiley, 1984. URL: https://resolver.caltech.edu/CaltechBook:1984.001.

[29] I. C. et.al. *Searches for neutrinos from cosmic-ray interactions in the Sun using seven years of IceCube data*. 2019. arXiv: 1912.13135 [astro-ph.HE].

[30] K. Abe, J. Adam, H. Aihara, T. Akiri, C. Andreopoulos, S. Aoki, A. Ariga, T. Ariga, S. Assylbekov, D. Autiero, M. Barbi, G. Barker, G. Barr, M. Bass, M. Batkiewicz, F. Bay, S. Bentham, V. Berardi, B. Berger **and** J. Zmuda. "Precise Measurement of the Neutrino Mixing Parameter $\theta_{23} fromMuonNeutrinoDisappearanceinanOff - axisBeam$". **in**: *Physical review letters* 112 (**march** 2014).

[31] P. Adamson **andothers**. "Measurement of the neutrino mixing angle θ_{23} in NOvA". **in**: *Phys. Rev. Lett.* 118.15 (2017), **page** 151802. DOI: 10.1103/PhysRevLett.118.151802. arXiv: 1701.05891 [hep-ex].